Iron-rich slag addition in ternary binders of Portland cement, aluminate cement and calcium sulfate

Jennifer Astoveza, Romain Trauchessec, Sylvie Migot, Ratana Soth, Yiannis Pontikes

Iron-rich slag addition in ternary binders of Portland cement, aluminate cement and calcium sulfate

Jennifer Astoveza[a,b,c], Romain Trauchessec[b], Sylvie Migot-Choux[b], Ratana Soth[a], Yiannis Pontikes[c]

[a] Science and Technology Department, Imerys Technology Centre- Lyon, 38090 Vaulx-Milieu, France
[b] Institut Jean Lamour, UMR CNRS 7198, Université de Lorraine, ARTEM, 94 - 86 Rue Sergent Blandan, 54000 Nancy
[c] KU Leuven Department of Materials Engineering, 3001 Leuven, Belgium

jennifer.astoveza@imerys.com, romain.trauchessec@univ-lorraine.fr, sylvie.migot@univ-lorraine.fr, ratana.soth@imerys.com, yiannis.pontikes@kuleuven.be

Abstract

The growing demand for sustainability in the recent decades has driven the exploration for new supplementary cementitious materials (SCM) such as the non-ferrous metallurgy (NFM) slags. In this study, the hydration of an iron-rich NFM slag incorporated in CAC-PC-calcium sulfate ternary binders was investigated. The dimensional stability of mortars demonstrated the contribution of the slag addition in mitigating excessive expansion while maintaining an acceptable mechanical strength over 180 days. The degree of slag hydration estimated with X-ray Computed Tomography (XCT) support the activating effect of the PC, while isothermal calorimetry, XRD, TGA and ATR-FTIR were used to delineate the evolution of the phase assemblage. Finally, TEM-EDS revealed the incorporation of Fe in hydrate gels grouped into two clusters according to a Ca-Al-Si ternary diagram: (1) Al-rich gels in the formulation with no PC; and (2) intermixed hydrate gels associated with Ca, Al and Si in the formulations with PC.

Keywords

calcium aluminate blended cement, slag hydration, CAC, SCM, TEM-EDS, ATR-FTIR, hydrate gels

1 Introduction

The ternary binder consisting of ordinary Portland cement (PC), calcium aluminate cement (CAC) and calcium sulfate (C$) is primarily used in rapid repair applications such as in tile adhesives and self-levelling underlayment (SLU) [1–3]. The rapid setting, fast strength development and shrinkage compensation properties are associated to the ettringite formation in the first hours of hydration resulting from the immediate reaction of monocalcium aluminate from the CAC and C$ [4]. In high volume

applications, the incorporation of PC is essential in contributing to the long term strength properties [5] while reducing the total cost [6] of the binder.

Previous studies [4,6–8] in such ternary binders have provided a fundamental understanding of the hydration mechanism governing the system. Bizzozero and Scrivener (2014) enumerated the hydration reactions and discussed their kinetics by following the phase assemblage evolution over time [6]. Their study demonstrated the formation of ettringite and gibbsite, principally in the early days, from the hydration of monocalcium aluminate and C$ according to **Equation 1**[1]. PC could further contribute to this initial ettringite formation by providing additional Ca^{2+} ions in a reaction described in **Equation 2**. When sulfates are depleted, the conversion of ettringite to monosulfoaluminate could be triggered in a system where aluminates are still abundant (**Equation 3**). C-S-H can also be formed from the hydration of the main phases of PC along with other minor components (i.e. hydrogarnet, strätlingite, monocarboaluminates) in the later hydration age. Additionally, the studies by Torréns-Martin et al., (2013) and Nehring et al., (2018) highlighted the significance of the CAC/C$ and PC/CAC ratio not only in defining the hydrate phase assemblage of the system but also the kinetics of hydration [7,8].

$$3CA + 3C\$H_X + (38 - 3x)H \rightarrow C_3A \cdot 3C\$ \cdot H_{32} + 2AH_3 \qquad \textbf{Equation 1}$$

$$3CA + 9C\$H_X + 6CH + (90 - 9x)H \rightarrow 3C_3A \cdot 3C\$ \cdot H_{32} \qquad \textbf{Equation 2}$$

$$C_3A \cdot 3C\$ \cdot H_{32} + 2C_3A + 4H \rightarrow 3C_3A \cdot C\$ \cdot H_{12} \qquad \textbf{Equation 3}$$

Despite numerous studies relating to this ternary binder system, the preceding investigations mostly explored PC-rich formulations typically representing between 70-85 wt% of the binder in the dry mix. Although a PC-rich blend is perceived to be more relevant to the industrial high volume applications primarily due to cost considerations, the adaptability of CAC-rich blends remains beneficial in specialized applications along with a conceivable environmental advantage. For instance in self-levelling flooring applications, CAC-rich dry mixes could be developed to better maximize the self-drying[2] capacity of the CAC component [9]. With this property, there is a shorter waiting time dedicated

[1] Cement shorthand notation used for Equations 1-3 : C: CaO, A: Al_2O_3, $: SO_3, H: H_2O. Also, x is equal to 2 for gypsum, 0.5 for hemihydrate and 0 for anhydrite

[2] The ability of the binder to fully consume the mix water for hydration, in this case, related to ettringite formation

for the evaporation of the excess mix water prior to flooring installation. While in terms of sustainability, a Life Cycle Assessment (LCA) comparing blends for SLU flooring mortars [10] has previously demonstrated that CAC-rich ternary binders could yield lower carbon footprint as opposed to an equivalent volume of PC-rich ternary blend while maintaining a comparable strength performance.

When added in lower proportions (10-30 wt%), PC could be a mineral activator for slag (GGBFS) in CAC systems [11,12] not only by increasing the alkalinity of the pore solution but also by contributing ions that can influence the formation of hydrates. Thermodynamic modelling indicates pH values greater than 12 in pore solution of typical PC hydration [13]; whereas a pH less than 12 is expected for CAC-dominated systems even reaching 10.5 with excess C$ [14]. It has been reported [15] that a more stable ettringite is formed and GGBFS dissolution is increased at pH values greater than 12. Furthermore, the addition of PC contributes ionic species, such as Ca^{2+}, $Al(OH)^{4-}$ and SO_4^{2-}, that can influence the formation and stability of hydrates [14] and the dissolution of the slag [15].

There has been no previous investigation on the incorporation of non-conventional SCM such as non-ferrous metallurgy (NFM) slag in a CAC-rich ternary binder system for which the environmental benefits could be further maximized. To address this growing trend on the valorization of industrial residues [16,17] in various applications particularly in cement binders, the preceding publications [18,19] of the authors introduced the properties of a CAC-rich binder incorporating an iron (Fe)-rich slag as SCM. These studies confirmed the long term reactivity of the slag (>28 days) with a hydration degree reaching up to 49% after 1 year of curing quantified using X-ray computed tomography (XCT) [18] . Despite the successful preliminary study, obtaining high early (<28 days) strength remains critical in CAC fast-repair applications prompting the challenge on improving the kinetics and the overall extent of slag hydration. Consequently, a better understanding on the hydration reactions governing the slag hydration is warranted with the ultimate goal of establishing an effective activation technique. While on a theoretical perspective, a deeper investigation is also oriented towards demonstrating the fate of Fe, the main component of the slag, during the hydration.

This study is directed towards bridging the aforementioned gaps while providing a novel outlook on the use of an Fe-rich slag coming from a lead-zinc plant in CAC-based binders incorporating PC. Three formulations containing 30 wt% of the slag were prepared with varying CAC/HH ratio and PC content.

First, the mechanical strength (EN-196-1) and dimensional stability of these formulations were followed over time. The slag hydration degree was then quantified using XCT while the phase assemblage evolution was characterized using XRD, TGA and Attenuated Total Reflectance – Fourier Transform Infrared Spectroscopy (ATR-FTIR). Finally, the fate of Fe during slag hydration was deduced based on Transmission Electron Microscopy (TEM).

2 Materials and Methods

This study utilized the same batch of raw materials from a preceding investigation, Astoveza et al., 2020 [18]. An Fe-rich NFM slag originating from a pilot-scale testing in a lead-zinc plant was added in dry mix formulation of CAC (Secar® 51) and calcium sulfate hemihydrate (HH, Prestia Selecta). The slag is 92 wt% amorphous balanced by 8 wt% wüstite (FeO) in the crystalline fraction. The CAC is dominated by monocalcium aluminate (CA) comprising >60 wt% of the mineral assemblage while the minor components include gehlenite (C_2AS), belite (C_2S), perovskite (CT) and spinel ($MgAl_2O_4$). Similarly, Millisil E400® is used as the "quartz filler" in the reference formulations to distinguish the physical effect of the slag substitution. In addition to these materials previously characterized in the aforementioned publication, a PC (CEM I, 52.5R Milke® Premium by Heidelberg Cement) was included in the new binder system investigated in this study. The chemical composition of the raw materials presented in **Table 1** was measured using semi-quantitative Bruker S4 Pioneer X-ray fluorescence (XRF). The density was measured through helium displacement using the Micrometrics AccuPyc II 1340 pycnometer system. Particle size distribution and specific surface area presented in **Table 2** were determined using the Malvern Mastersizer 3000 laser diffraction system and both a semi-automatic Blaine Air Permeability Apparatus and the Micrometrics BET Tristar 3000, respectively. The XRD pattern of the PC used acquired using D8 Advance X-ray Diffractometer (XRD) from Bruker coupled with LynxEye detector is shown in **Figure 1**. A scan ranging from 5 to 80° was made at the 2θ using CuK_α (1.54 Å) radiation and a step size of 0.02°. DiffracEVA and TOPAS software were used for the phase identification and quantification of the raw materials' composition, respectively. The amorphous content of the raw slag was determined by applying the method described in Srodon et al.,

2001 [20] where 10 wt% of analytical grade zincite is added as an internal standard during sample preparation.

Table 1 Assay and density of the raw materials used where " – " indicates the absence of measurement due to their anticipated negligible value, while "<dl" indicates that the measurement is below the lower detection limit of the device (modified from [18])

	slag	PC	CAC	HH	quartz filler
Density, g/cm^3	3.67	3.11	3.02	2.64	2.66
Amorphous content, wt%	92	–	–	–	–
Chemical composition, wt%					
CaO	13.6	67.1	37.7	41.7	<dl
Al_2O_3	5.2	3.9	52.3	0.1	<dl
SiO_2	28.1	20.9	4.9	0.8	99.8
FeO (slag); Fe_2O_3 (others)	41.4	1.4	1.8	0.1	<dl
MgO	2.4	0.7	0.4	0.1	<dl
SO_3	0.8	4.3	0.2	56.5	<dl
K_2O	0.7	0.8	<dl	<dl	<dl
P_2O_5	0.2	0.1	0.1	<dl	<dl
Na_2O	4.3	0.3	<dl	<dl	<dl
Cr_2O_3	0.1	<dl	0.1	<dl	<dl
CuO	0.4	<dl	<dl	<dl	<dl
ZnO	<dl	<dl	<dl	<dl	<dl
Others	2.8	0.5	2.5	0.7	0.2

Table 2 PSD and specific surface area of the raw materials (modified from [18])

	Particle Size Distribution (µm)			Specific Surface Area	
	d10	d50	d90	Blaine (cm^2/g)	BET(m^2/g)
PC	0.9	8.5	25.3	3412	0.992
slag	1.1	7.9	50.5	4370	1.352
CAC	1.1	11.6	52.3	4270	1.019
quartz filler	1.2	12.4	40.6	4580	1.118

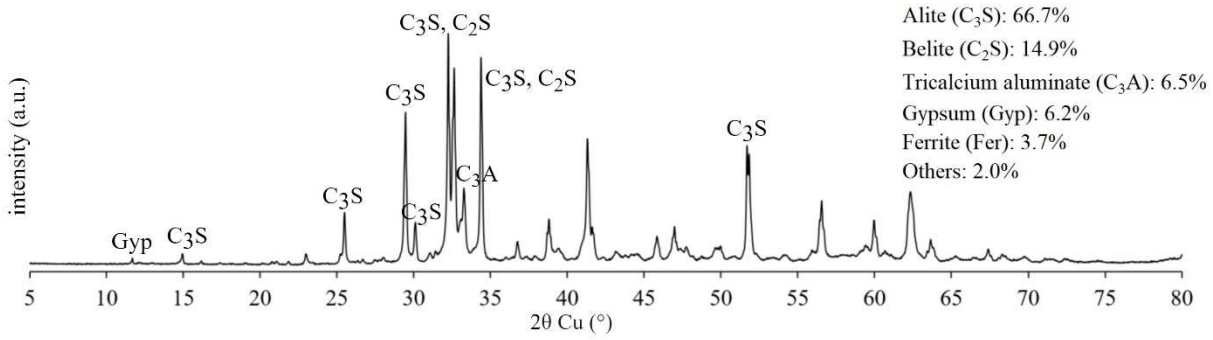

Figure 1 XRD pattern of the raw Portland cement (Milke premium 52.5R by Heidelberg Cement) following the abbreviations: alite (C_3S), belite (C_2S), tricalcium aluminate (C_3A) and gypsum (Gyp)

The ATR-FTIR measurements were made using Bruker Alpha-P spectrometer with diamond crystal. Each measurement (average of 3 runs per sample) consisted of 32 scans with a resolution of 4 cm^{-1} and a range from 380 to 4000cm^{-1}. The raw results were expressed in transmittance and were then converted to absorbance for the analyses. The measurements presented in **Figure 2** demonstrate the complex spectra [21] of the CAC consisting of Si-O (around 1030 and 415 cm^{-1}) and various Al-O peaks (between 521-786 cm^{-1}). On the contrary, the slag only shows Si-O-T (where T could be Al, Fe or Si) asymmetric stretching vibrations of the mode v3 (900 cm^{-1}) and Si-O-T asymmetric bending vibrations of the mode v4 (rocking) at 470 cm^{-1} similar to the characteristics of the Fe-rich slag presented in Siakati et al., 2020 [22]. The HH spectrum shows distinct S-O peaks at: 1150 and 1115 cm^{-1} (mode v3), 1006 cm^{-1} (mode v1), 653 and 593 cm^{-1} (mode v4); and O-H peaks at 1620 cm^{-1}, 3660 and 3550 cm^{-1} (mode v2, v3 and v1 respectively) [23]. Finally, two main peaks are manifested by the raw PC sample at 880 cm^{-1} and 520 cm^{-1} attributed to the overlapping double peak of Si-O asymmetric stretching vibration bands of C_3S and C_2S [24].

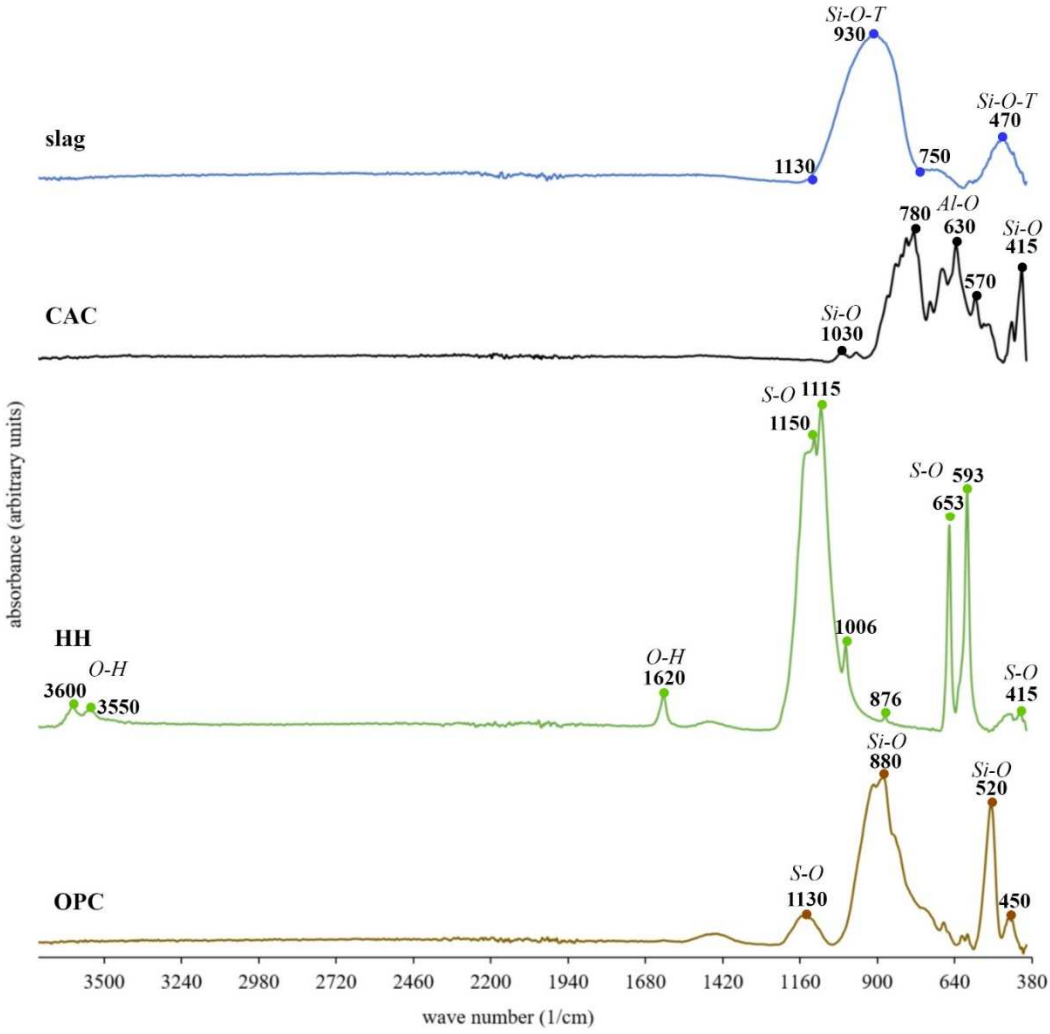

Figure 2 ATR-FTIR spectra of the raw materials

Three formulations incorporating 30 wt% slag and a varying proportion of PC, CAC and HH shown in **Table 1** were investigated in this study along with their respective reference formulations. Formulation (A) 1.6CAC-HH is a ternary CAC-HH-slag binder similar to the slag-containing formulation investigated in the preceding publications [18,19] but with a lower CAC/HH ratio (from 4.5 to 1.6). On the other hand, formulations (B) 1.6CAC-HH-30PC and (C) 4.5CAC-HH-30PC are quaternary CAC-HH-slag-PC binders both containing 30 wt% of PC but with varying CAC/HH ratio at 1.6 and 4.5, respectively. The selection of these mixed designs aimed to simultaneously represent low and high sulfate systems, evaluating its impact on the hydrate phase assemblage and its influence on the reactivity of the slag. It was decided that 30 wt% of slag addition compromises the expected reduction in mechanical strength observed in previous investigation [18] while still being significant enough to demonstrate a discernible influence, if any, especially on the chemical properties of the binder.

144 A constant amount of citric acid was used as an admixture in order to delay the setting thereby providing
145 the needed time-window to place the mixtures in the molds. A study by Nguyen et al., (2019) reported
146 that the addition of such low amount of citric acid (0.1-0.5 wt%) has no clear influence on the phase
147 assemblage evolution throughout the cement hydration [25]. Paste formulations were prepared in a batch
148 of 100 g dry mix formulation using a water to binder (w/b) ratio of 0.6. Mixing was performed for 2 min
149 using an electric agitator at 250 rpm directly after water addition. The mixtures were then proportioned
150 into smaller 30 ml molds individually designated to represent a curing time, sealed and agitated in a
151 Turbula® mixer for about 7-8 minutes until the initial hardening. This protocol aims to hinder
152 preferential segregation of the high density slag at the bottom of the containers, thereby promoting
153 representative sampling for the subsequent analyses. Addressing this problem with agglomeration of
154 slag particles during curing was discussed in the authors' preceding work [26]. The samples were left to
155 age in their sealed containers for 1, 7, 28 and 165/180 days in a 20°C room. At each predefined curing
156 age, hydration was stopped through solvent exchange using isopropanol as described in the previous
157 publication [18].
158 Mortar samples for mechanical strength test were prepared following the same formulation as the paste
159 samples (**Table 3**) for the binder component albeit using a w/b ratio of 0.5 and following the EN-196-1
160 protocol for making standard mortars. After curing for 24 h in a chamber with 20°C and 95% relative
161 humidity, the mortars were demoulded and cured under water using individual 20 L plastic buckets each
162 containing maximum of 3 mortars of the same formulation. The containers were filled with deionized
163 water, sealed and stored in a 20°C (AFNOR) room. Moreover, reference mortars (cement and filler
164 reference) were made following the formulations presented in **Table 3**. The compressive and flexural
165 strength of the mortars were determined according to the EN-196-1 standard after 1, 7, 28 and 165/180
166 days of hydration. Using the strength values obtained from filler-replaced mortars as the reference, the
167 "deviation from the filler reference" was calculated as the difference between the strength values of the
168 slag-containing mortar and its corresponding filler reference divided by the former. Expressed in
169 percentage, this value could be one of the possible indications of slag reactivity while distinguishing
170 the "filler effect" [27] advantage to strength evolution with the SCM addition. For the same standard
171 mortar samples cured under water, length variation was followed over time using an extensometer

having installed gauge studs during moulding. Additionally, Walter+Bai shrinkage test (device type SWG-H-400) was performed on 70 x 70 x 70 mm^3 (initial length 400 mm) triangular prism mortars to follow the dimensional variation of the three formulations over 100 h of air curing at 20°C.

Table 3 The paste composition (in wt%) of the three slag-containing formulations investigated in this study along with their corresponding reference formulations. The cement reference contains no slag while the filler reference utilized the equivalent volume of quartz filler to replace the slag. Both of these references preserve the ratio of the CAC and HH components as shown.

formulation	slag	quartz filler	citric acid	PC	CAC	HH	CAC/HH ratio
slag-containing							
(A) 1.6CAC-HH	30	0	0.3	0	43	27	1.6
(B) 1.6CAC-HH-30PC	30	0	0.3	30	25	15	1.6
(C) 4.5CAC-HH-30PC	30	0	0.3	30	33	7	4.5
cement reference (no SCM)							
(A) cement reference	0	0	0.3	0	61	39	1.6
(B) cement reference	0	0	0.3	43	36	21	1.6
(C) cement reference	0	0	0.3	43	47	10	4.5
filler reference (with quartz filler)							
(A) filler reference	0	24	0.3	0	47	29	1.6
(B) filler reference	0	24	0.3	33	27	16	1.6
(C) filler reference	0	24	0.3	33	36	8	4.5

The degrees of slag hydration after 28 and 180 days of curing derived from a combination of XCT (Phoenix Nanotom S, GE Inspection Technologies X-ray computed tomography system) and volume analysis (Bruker CT-Analyser) are deduced after following the methodology detailed in the preceding publication [18]. This technique calculates the degree of slag hydration by associating it to the change in the total volume occupied by the slag particles as hydration proceeds. This methodology assumes that the dissolved slag completely participates towards the formation of hydration products. A 3 x 3 x 3 mm^3 cubic volume inside each hardened paste sample is selected for the scan operating at 90 KV and 170 µA with an isotropic voxel resolution set to 2.15 µm. For this technique, the hydration of the paste samples is continuous (no solvent exchange) in an attempt to follow the dissolution of the slag particles

consistently in the same volume. It must be noted however that in this calculation, the base value (zero reactivity) used was the total slag volume obtained at 1 day. This means that any slag dissolution during the first 24 h of hydration is assumed to be negligible supported by the observations from the preceding publication and therefore not accounted for in the quantification.

Early hydration reactions were characterized by following the heat release during the first 7 days of freshly mixed paste samples through isothermal calorimetry (TAM Air, TA instruments) at 20°C. Long term hydration was examined using XRD and ATR-FTIR of hydrated paste samples following the same parameters described earlier for the characterization of raw materials. In addition to above, the evolution of the hydrate phase assemblages is followed through thermogravimetric analysis (TGA) under N_2 atmosphere from 30°-900°C heated at a rate of 30°C/min using the Mettler Toledo TGA/DSC Simultaneous Thermal Analyzer. Bound water content is assumed to correspond to the water loss measured between 50-500°C. Finally, a CM200 transmission electron microscope (TEM) equipped with an EDS Si (Li) EDAX system was used to examine several individual phases in the goal of characterizing the hydrate phase/s incorporating iron, the main component of the slag. For the sample preparation, the finely ground (<100 µm) powder of hydrated pastes after solvent extraction was dispersed in acetone solution. A droplet was extracted from the dilute suspension and placed on a 3 mm (diameter) grid with carbon film and allowed to dry. The fate of iron in these formulations is expected to provide an initial outlook on the hydration mechanism of similar Fe-rich SCM in CAC-based binder systems.

3 Results and Discussions

3.1 Physical properties

The mechanical strength (primary axis) of the standard mortars and the percentage deviation from their corresponding filler references (secondary axis) are presented in **Figure 3**. As expected, the lower amount of cement in the SCM-containing mortars has generally resulted in reduced strengths relative to their cement references, especially in the early days of hydration. However, this gap versus the cement reference is diminished over time for the slag-containing mortars which could be perceived as one of the indications of the slag's reactivity at long term. On the other hand, the rate of strength increase versus

the filler references could signify the potential role of the slag in the first 7 days of curing beyond that of an inert filler. The slag-containing binders are able to display rapid setting and hardening properties while attaining compressive strengths of more than 20 MPa just after 1 day of curing, and reaching as much as 50 MPa after 28 days, all while containing only between 40-60 wt% cement (PC and CAC). This could already be considered as a remarkable performance given that: there was no extensive mix design optimization performed to determine the ideal proportion of each component; the w/b ratio was kept at 0.5 to follow the EN-196-1 standard; and that the admixture used was limited to citric acid. While this progression continues towards 28 days of curing for the PC-containing formulations (B and C), the rate of strength development of the formulation without PC (A) stagnates as opposed to its filler reference. This can be associated to the rapid strength development property of CAC-dominated formulations whereby the final strength can be achieved even as early as after 1 day of curing [7,28]. Another study [6] on a similar ternary (PC, CAC, calcium sulfate) binder system, reported that PC is less reactive in the early hydration and only contributes to the long term strength and thus the continuous trend even beyond 28 days of curing.

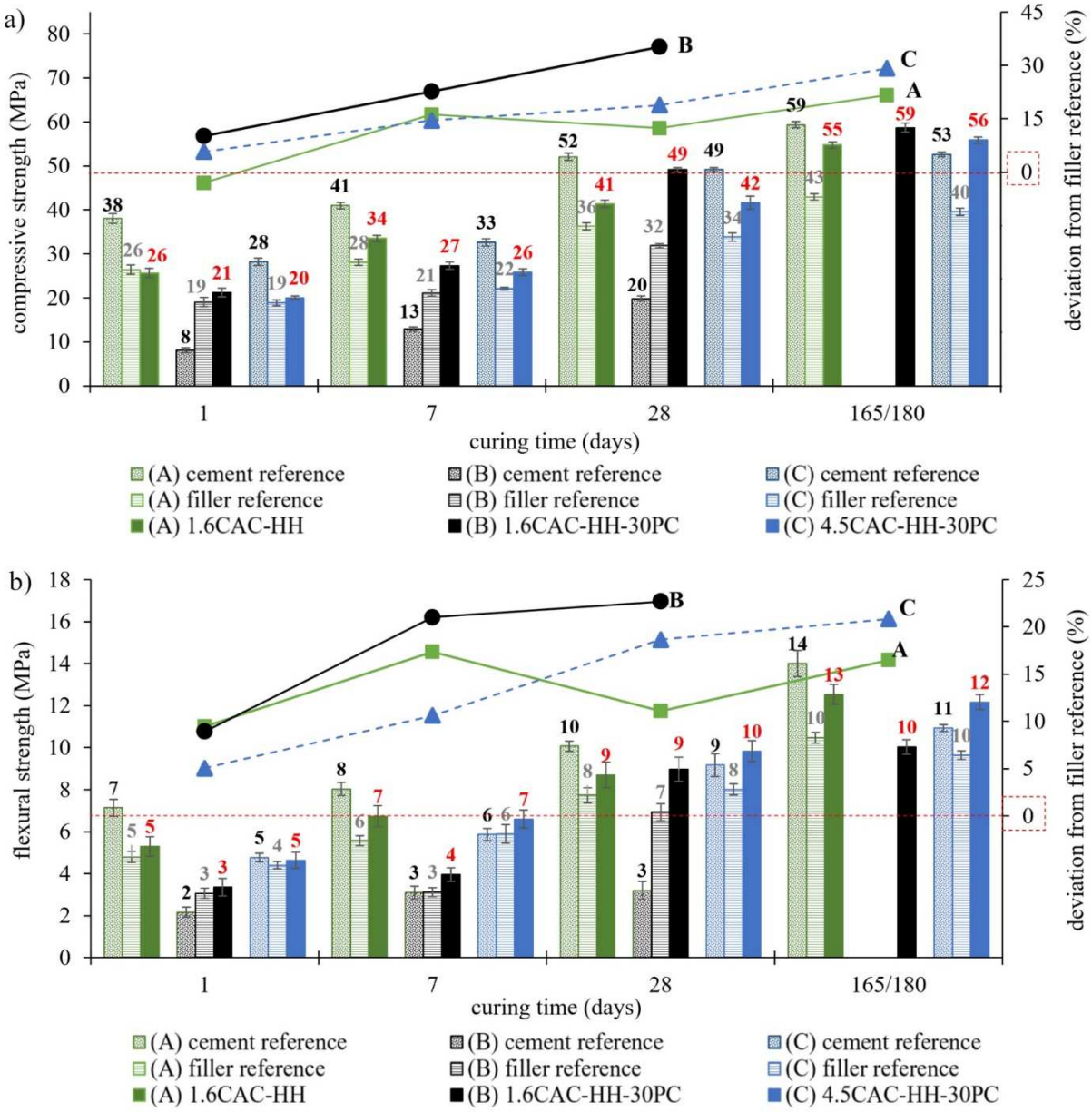

Figure 3 On the primary axis: the evolution of (a) compressive strength and (b) flexural strength of standard mortars where error bars represent standard deviation among 3 mortar samples. On the secondary axis, the percent deviation of the measured strength of the slag-containing formulations versus their corresponding filler reference. The strength values of the slag-containing mortars are shown in red font for emphasis.

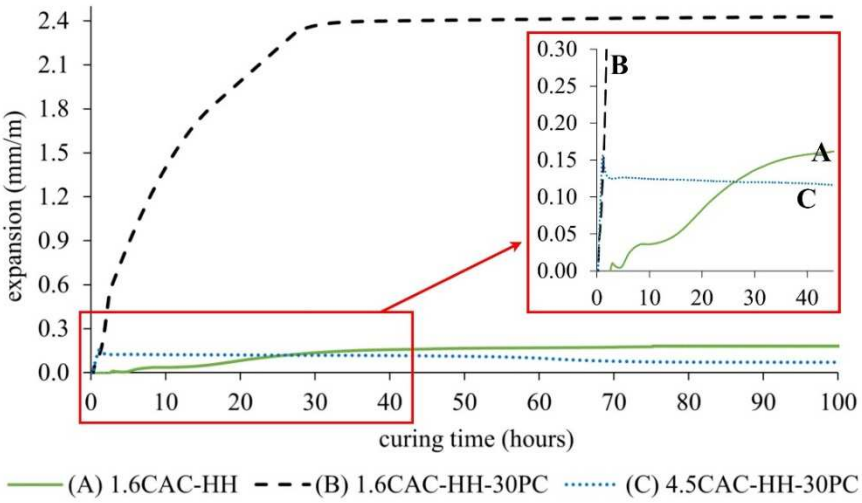

Figure 4 Dimensional stability of the three formulations measured using the Walter+Bai shrinkage test for air-cured samples during 100 h of hydration at 20°C. The insert graph provides a closer look at the trends during the early hydration

The highest rate of strength development among the slag-containing mortars relative to their respective references was attained by formulation B. On the contrary, this high sulfate ternary binder also yielded the highest expansion degree during the dimensional stability (Walter+Bai) test shown in **Figure 4**. Over expansion was observed in the references of this formulation which led to the disintegration of the mortars. It is important to mention that after approximately 30 days of curing under water, macro cracks started to appear on the cement reference of formulation B and these progressively became more apparent at later ages. The length variation of these mortars are presented in **Figure 5**b below. Both the reference mortars (no SCM and filler-replaced) manifested excessive expansion at later curing ages eventually making it impossible to perform further measurements for dimensional stability and strength test on these samples. On the contrary, no visible macro cracks were noted for the slag-containing mortars even beyond 45 days of curing under water. The slag appears to marginally mitigate the destructive expansion mainly resulting from the hydration of the more reactive components (CAC, HH and PC). Nevertheless, the low CAC/HH ratio (1.6) of the formulation B in combination with the selected proportion of the PC is considered to fall within a high risk zone for destructive expansion. This supports the importance of optimizing not only the CAC/HH ratio but also their proportion to PC similarly suggested in previous studies on ternary PC-CAC-calcium sulfate systems [6,7,28].

Unlike formulation B, formulations A and C demonstrated better dimensional stability during the Walter+Bai test. Slow progressive expansion spanning throughout the first 35 h of hydration was observed in formulation A. The higher HH content corresponding to the lower CAC/HH ratio of formulations A and B effectively prolonged their setting time (additional ≈14 minutes prior to final set). Conversely, the higher CAC content in formulation C resulted in rapid setting with the maximum expansion and dimensional stability already attained just within the first 2 h of hydration.

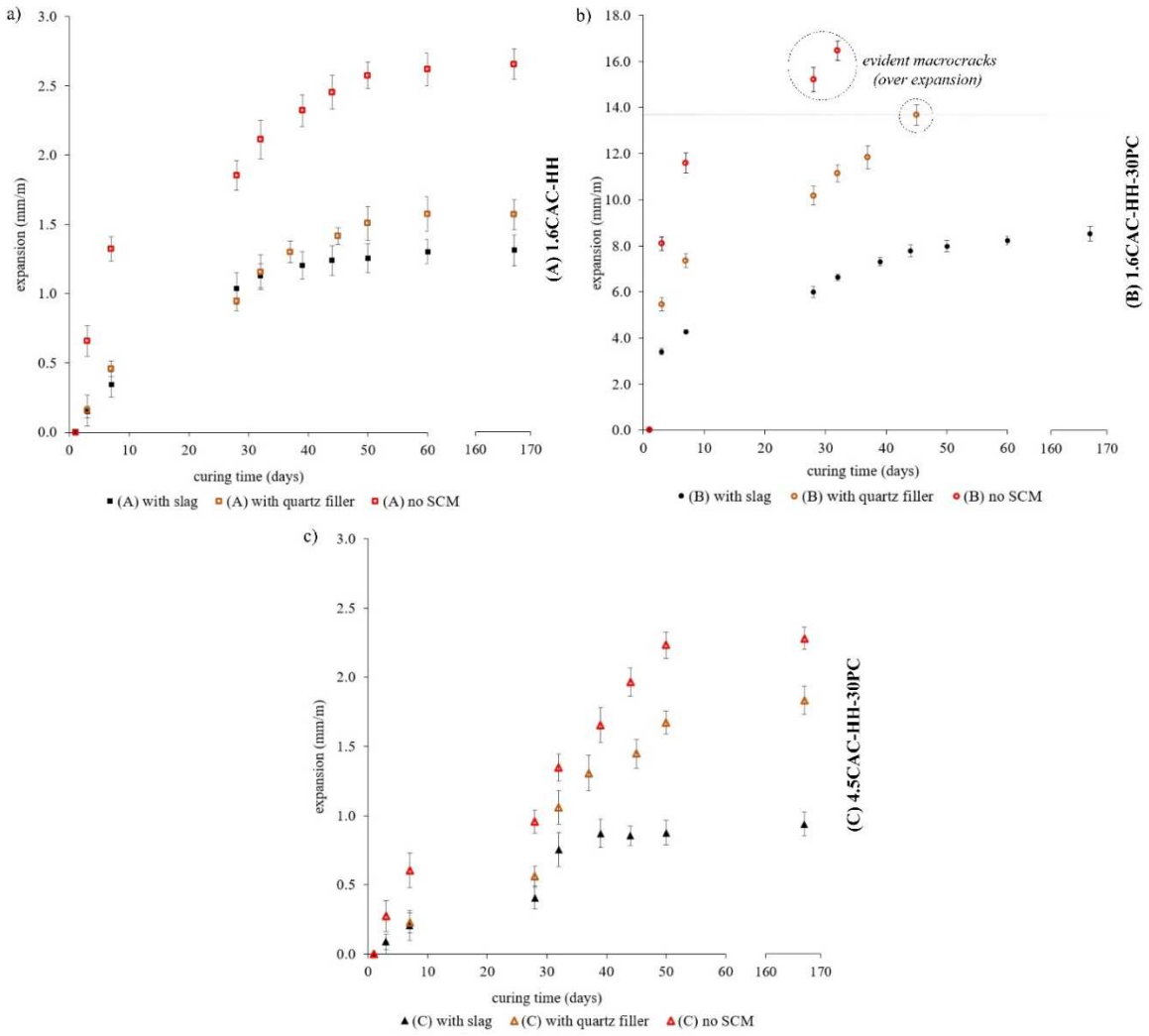

Figure 5 Length variation of standard mortars for the three formulations (with slag) and their corresponding reference mortars: filler reference (with quartz filler) and cement reference (no SCM) cured under water at 20°C

3.2 Degree of slag hydration

After 28 and 180 days of hydration, the degree of slag hydration estimated using a combination of XCT and volume analysis is presented in **Figure 6**. In the first 28 days of hydration, the general trend shows that the slag appears to be more reactive in the formulations containing PC (B and C) reaching as much as 17.4%, twice as high compared to the original formulation [18]. This confirms the contribution of the PC in improving the reactivity of the slag, which could be linked to the increase in alkalinity of the system [11,13,14] and to the additional ions released (predominantly Ca^{2+}) that could influence the hydration [12,14,15].

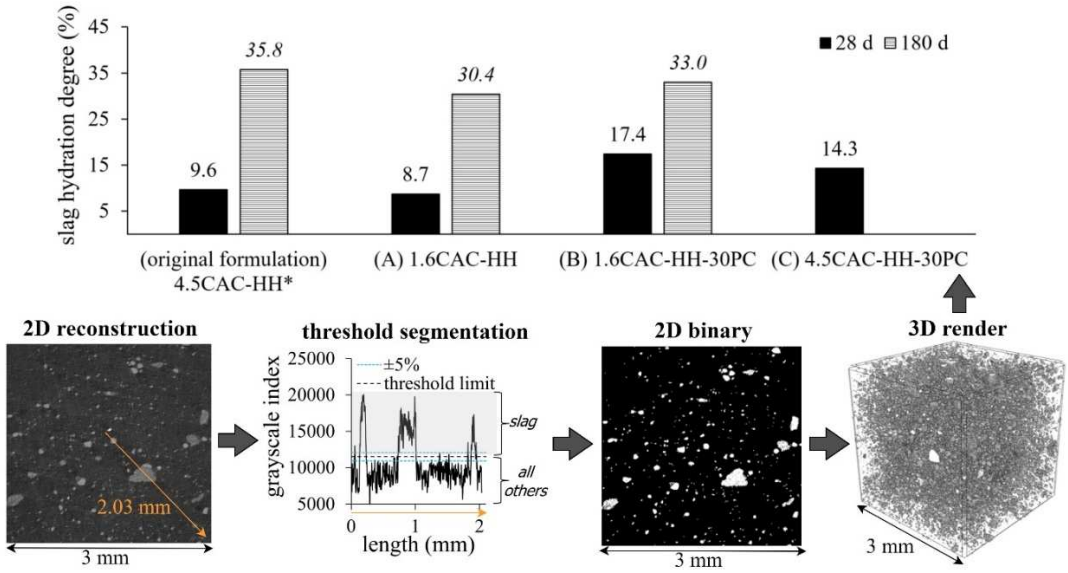

Figure 6 The degree of slag hydration derived using a combination of XCT and volume analysis applying the same methodology published in Astoveza et al., 2020 [18]. Illustrated in this figure are the major steps in the estimation including: (1) the 2D reconstruction of the scans; (2) threshold segmentation to distinguish the slag particles; (3) 2D binary images based on the previous step; and (4) generation of the 3D volume render where the degree of hydration was calculated from

On the contrary, the effect of the CAC/HH ratio to the degree of slag hydration remains inconsistent. For the blends without the PC, it appears that there was no significant difference in the slag reactivity regardless of the CAC/HH ratio. On the other hand, the increase in the HH content in the blend (lower CAC/HH ratio) containing 30 % PC appear to have contributed to the reactivity of the slag. The trends observed here are consistent with the strength evolution of mortars presented in the preceding section. In the first 28 days, strength development was more notable for the PC containing formulations but this

289 was reduced towards 180 days of hydration. This suggests that the activating effect of the PC addition
290 could be limited to the early-stage (<28 days) of hydration. More evidence to support this will be
291 discussed in the succeeding sections.

292 **3.3 Early hydration reactions**

293 The early age of hydration is described through the heat flow and cumulative heat release obtained from
294 isothermal calorimetry shown in **Figure 7**. Formulation A, the only binder among the three without PC,
295 exhibited two main hydration peaks determined in the previous studies [14,18] to correspond to the rapid
296 dissolution of hemihydrate leading to gypsum precipitation (first peak at around 1 hr) and the massive
297 ettringite and AH_3 precipitation (second peak before 3 h). The third peak observed in the original
298 formulation (4.5CAC-HH) [18] associated to the formation of monosulfoaluminate as the sulfate source
299 is depleted, is not detected in the first 7 days of hydration. This is a clear initial indication that the higher
300 HH content of the formulation A compared to the original formulation shifted the hydrate phase
301 assemblage from a monosulfoaluminate-dominated to an ettringite-rich system. The rapid formation and
302 the stability of ettringite in this formulation is further reflected by the fast increase in the cumulative
303 heat release release in **Figure 7**b. It can be seen that the maximum heat was achieved by the formulation
304 A at a faster rate compared to the formulations B and C both containing 30 wt% of PC. On the contrary,
305 periods of stagnation in the increase of the cumulative heat release were noted in the PC-containing
306 formulations before the final total heat is achieved. This can be explained by the mechanism of ettringite
307 barrier layer formation proposed in Torréns-Martin, Fernandez-Carrasco et al., 2013 [7] suggesting that
308 the ettringite layer formed around the anhydrous grains provisionally delays the silicates (mainly C_3S
309 and C_2S) hydration. The barrier formation is proposed to have a retarding effect to the diffusion process
310 such that momentary plateaus (**Figure 7**b, see formulations B and C) are visible in the cumulative heat
311 release curves. The heat continues to increase only when these barrier layers are broken during the
312 conversion of ettringite to monosulfoaluminate. This reaction can happen in multiple stages, one among
313 which is attributed to the broad peaks observed for formulations B and C in **Figure 7**a commencing at
314 around 8 h and 4 h respectively. Furthermore, the difference in the hydration mechanism between the
315 PC-containing formulations (B and C) is evident in the heat flow curve with the formulation B yielding
316 3 distinct peaks as opposed to the 2 main peaks of the latter. The complexity of the blends makes it

317 difficult to distinguish the overlapping peaks and associate them to specific reactions as the hydration
318 proceeds. In the end, it is evident that the incorporation of PC and the variation in the CAC/HH ratio
319 among these blends resulted in differences in the mechanism of early hydration reactions. At this point,
320 it is not clear whether these differences have an impact on the slag dissolution in the first hours of
321 hydration.

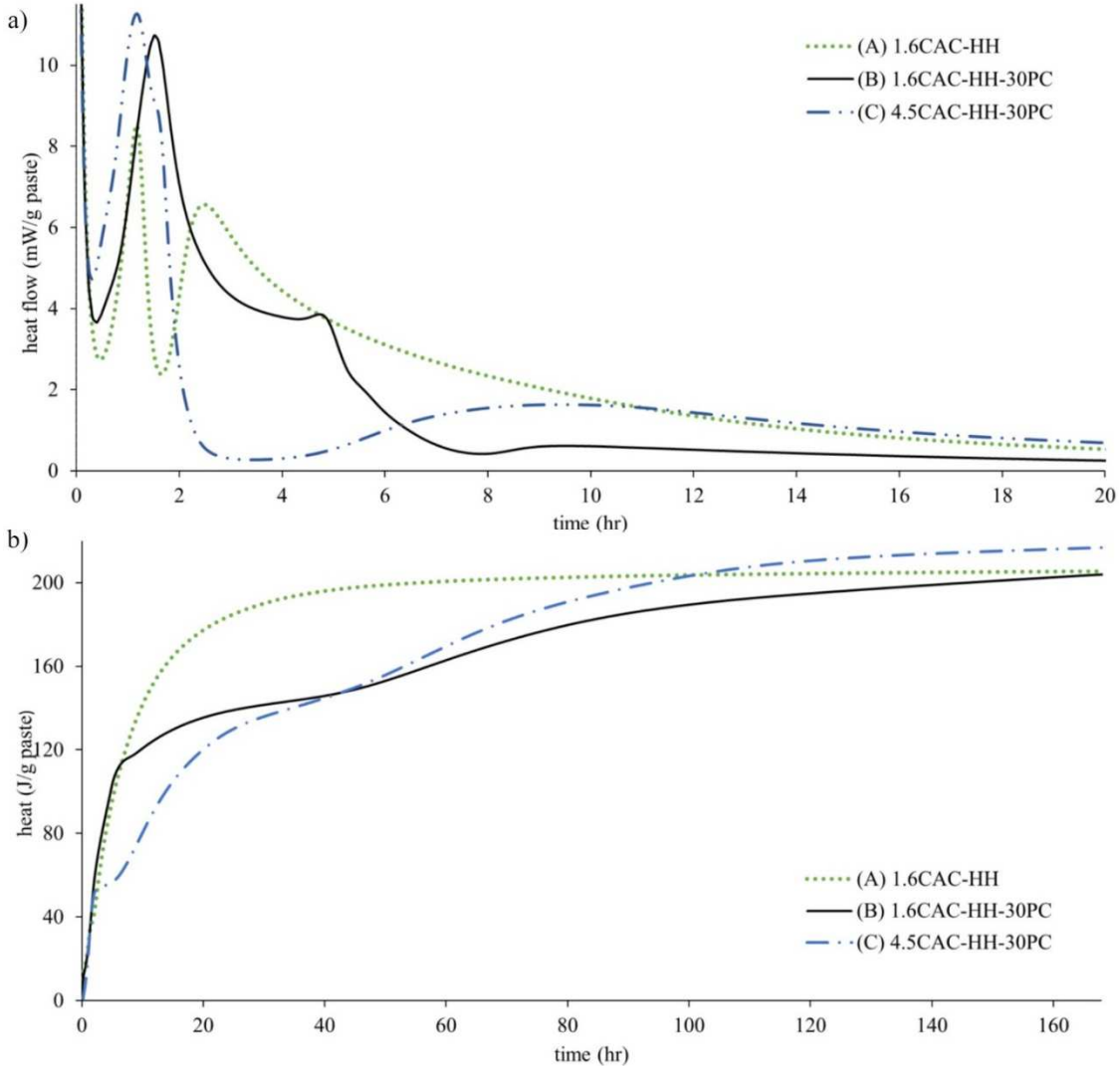

322

323 **Figure 7** (a) Heat flow and (b) cumulative heat release per gram of paste measured ex-situ using
324 isothermal calorimetry at 20°C

325 **3.4 Phase assemblage evolution over time**

326 To examine the phase assemblage evolution of hydrated paste samples, the results of XRD, TGA and
327 ATR-FTIR are presented and discussed in this section. These techniques consistently indicate that the
328 three formulations are governed by a hydrate system different from each other, briefly described below:

- **(A) 1.6CAC-HH** – dominated by ettringite and gibbsite throughout the curing period
- **(B) 1.6CAC-HH-30PC** – dominated by ettringite and gibbsite; strätlingite is increasing over time; possibly with C-S-H
- **(C) 4.5CAC-HH-30PC**– dominated by strätlingite and monosulfoaluminate; possibly with CSH

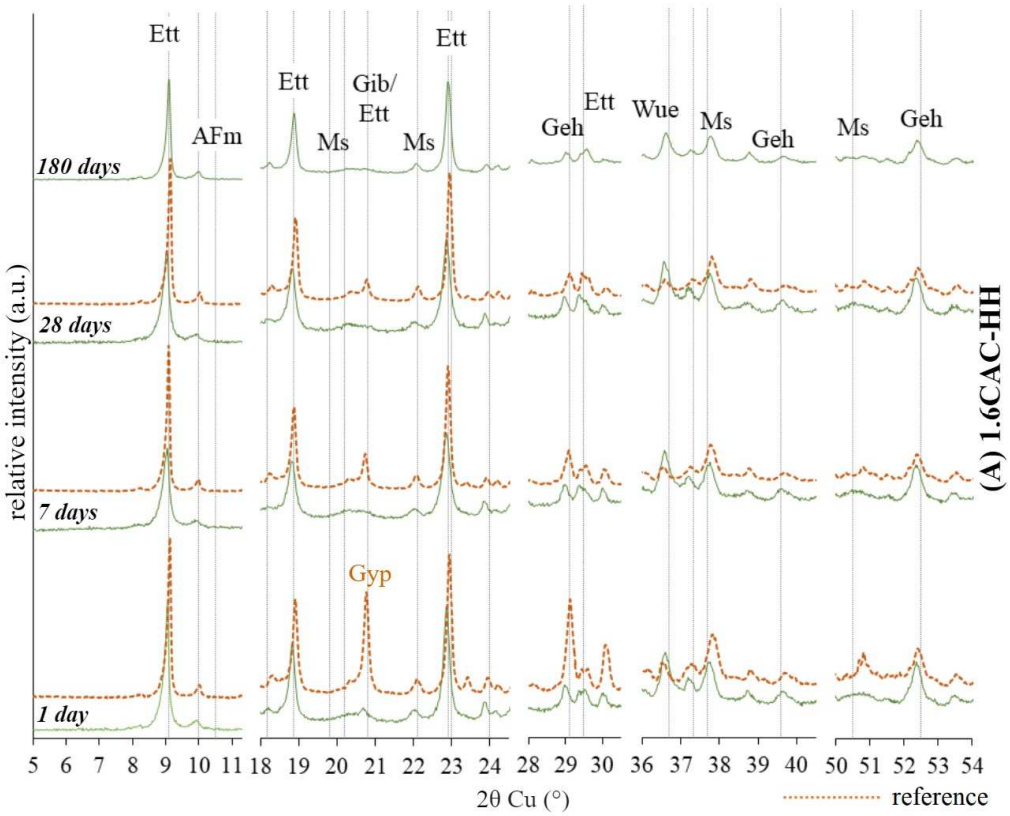

Figure 8 XRD patterns of formulation (A)1.6CAC-HH and its corresponding cement reference measured from paste samples after stopping the hydration at 1, 7, 28 and 180 days of curing. The different phases are abbreviated as follows: (Ett) ettringite, (AFm) AFm, (Ms) monosulfoaluminate, (Geh) gehlenite, (Gyp) gypsum and (Wue) wüstite.

From the XRD patterns in **Figure 8**, strong ettringite peaks are observed, resulting from the hydration of monocalcium aluminate, the main component of CAC, and the HH. Throughout the curing period, there was no apparent change in the patterns (nor indications of new Fe-containing hydrates) signifying the stability of the ettringite formed in this system and supporting the low reactivity of the slag (**Figure 6**) in the first 28 days of hydration. The results are consistent with the evolution of DTG curves (**Figure 9**) and the FTIR spectra (**Figure 12**) displaying steady ettringite signatures throughout the curing period.

Compared to the cement reference, the only notable difference is the less apparent peak associated to gypsum at $2\theta = 20.8°$ for XRD and at 160°C for DTG for the slag-containing formulations early in the hydration. While the presence of gypsum in significant proportion is not typical at this stage, this could be related to the previously observed [29–31] localized embedment of gypsum in confined aluminum hydroxide matrix. Gypsum and ettringite formed in the early hours of hydration could be wrapped around gels of aluminum hydroxide, inducing high supersaturation and could eventually lead to a buildup of crystallization pressure in confined matrices [32]. This process could be a relevant factor in explaining the higher expansion of the reference versus the slag-containing formulations in the first hours of hydration. However, the growth of crystals in confined space is not thermodynamically favored and eventually the gypsum dissolves and diffuses towards the open space [29]. From the XRD (**Figure 8**) and DTG (**Figure 9**) results, the gypsum signals diminish after 1 day of curing. The addition of the slag and the PC, could clearly influence this reaction as no similar signature of gypsum was detected for the other formulations. While more dimensionally-stable mortars were obtained with the addition of the slag, it could not be directly credited for the superior mechanical performance of formulation A versus those of the PC-containing formulations, B and C. Instead, the slow increase in the total bound water content (**Figure 9**) over time, consistent with the strength evolution, could indicate that the mechanical performance was more likely contributed by the hydration of CAC and HH resulting in a stable ettringite-dominated phase assemblage rather than this being a consequence of slag addition.

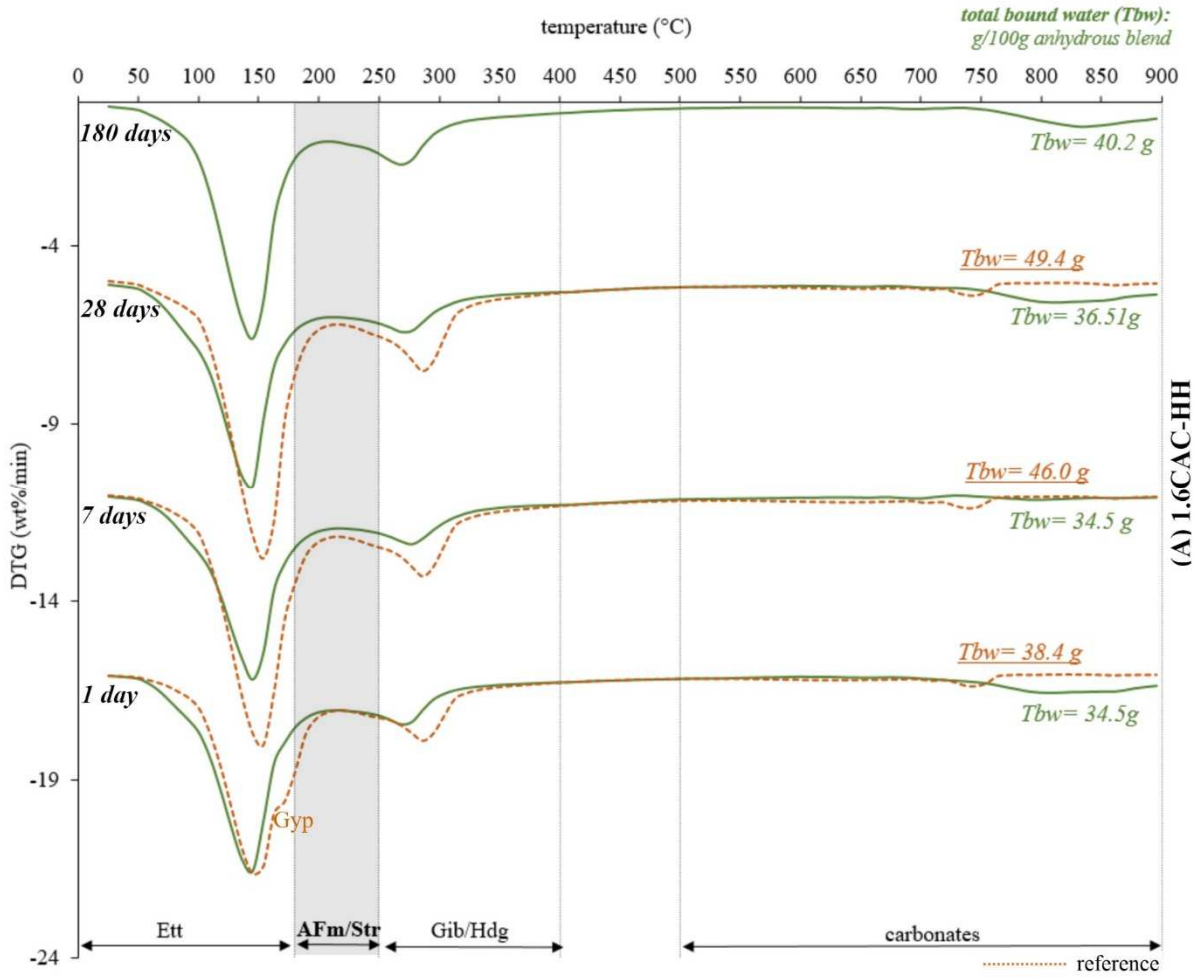

Figure 9 Evolution of the DTG curves of formulation (A)1.6CAC-HH and its corresponding cement reference measured from paste samples after stopping the hydration at 1, 7, 28 and 180 days of curing. The different phases are abbreviated as follows: (Ett) ettringite, (AFm) AFm, (Str) strätlingite, (Gib) gibbsite, (Gyp) gypsum and (Hdg) hydrogarnet

With the addition of the PC in the system, distinct changes in the patterns could be noted especially for the formulation (B) 1.6CAC-HH-30PC having the highest degree of slag hydration according to the XCT analysis (**Figure 6**). In this formulation, the changes were evident mainly from 1 to 7 days of hydration consistently observed among the three characterization techniques. For instance, in the XRD patterns we can see the appearance of the strätlingite peak at $2\theta = 7°$ and 21.2° after 7 days and the changes in the pattern in the peaks between 29°-30° where several silicate phases coincide. These changes could be relevant to slag reactivity considering the substantial role of the silicates from the slag, governing the formation of strätlingite and the consumption of gehlenite from the CAC [18]. It is clear

that the complex nature of the hydrate phase assemblage of the systems in this study, notably the presence of several amorphous phases, requires characterization techniques far beyond the conventional XRD and TGA techniques explored in the preceding study.

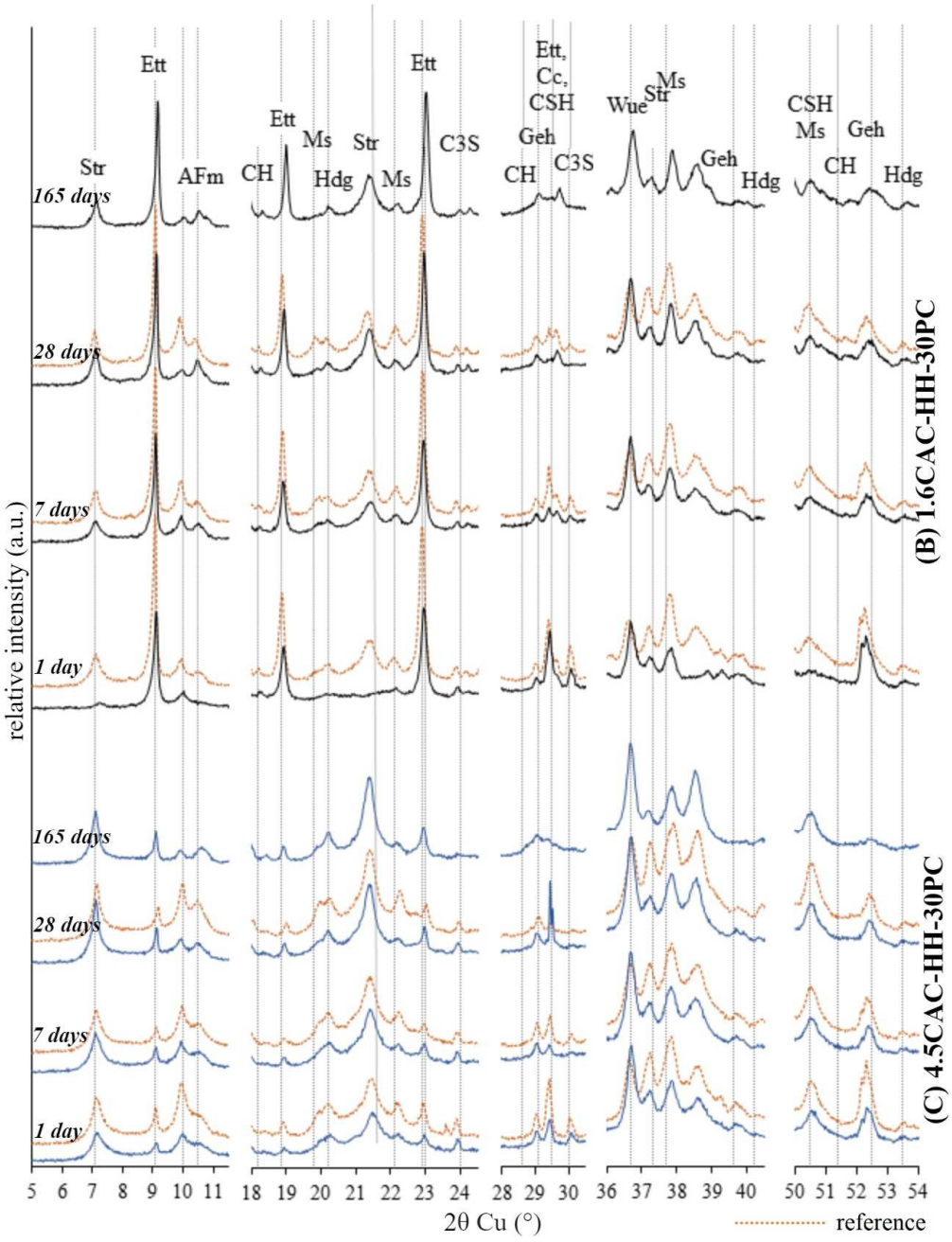

Figure 10 XRD patterns of formulations (B)1.6CAC-HH-30PC, (C) 4.5CAC-HH-30PC and their corresponding cement references measured from paste samples after stopping the hydration at 1, 7, 28

and 165 days of curing. The different phases are abbreviated as follows: (Str) strätlingite, (Ett) earmonosulfoaluminate, (C3S) alite, (Geh) gehlenite, (CSH) C-S-H, and (Wue) wüstite.

Although the DTG curves could give an indication on the evolution of the amorphous phases, the overlap of the ettringite and C-S-H region for instance poses a challenge in differentiating their individual contribution. Nonetheless, for the partly amorphous phases such as gibbsite in formulation B, the DTG curve remains helpful in indicating its presence at 1 day with the peak at around 270°C (**Figure 11**). This peak diminishing towards 7 days of curing suggesting gibbsite's dissolution and transformation into other hydrate phases. Whereas gibbsite is stable in the ternary binder of CAC-HH-slag such as in formulation A, the formation of CH in formulations B and C resulting from the hydration of PC destabilizes the gibbsite in the system. This is because CH and gibbsite cannot co-exist thermodynamically and thus favoring their dissolution with several possible reactions in function of the other phases present in the solution as reported in Bizzozero and Scrivener, 2014 [6]. In this case, it is most likely that the CH and gibbsite reacted with CH_x$ to form additional ettringite.

Another notable observation from the DTG evolution (**Figure 11**) of formulation B are the small variations in the peak position between 90° and 140°C where ettringite and C-S-H overlap. These deviations over time and between the slag-containing and the reference formulations indicate the difference in the proportions of the two hydrate phases in the samples. The peak shifts could also signal changes in the composition of the hydrates, particularly the C-S-H gel [33] that could be interpreted as an early indication of the nature of the Fe-bearing hydrate to be discussed in more detail with the results from the TEM-EDS analysis. Furthermore, the evolution of the total bound water content of the slag-containing formulation B differs from that of its reference formulation. Whereas the reference formulation appears to have quickly obtained its maximum bound water content in the first 7 days of hydration, the respective value for the slag-containing formulation continues to increase significantly for the slag-containing formulation throughout the observed period which could be another indication of the slag dissolution's effect on the hydration reactions.

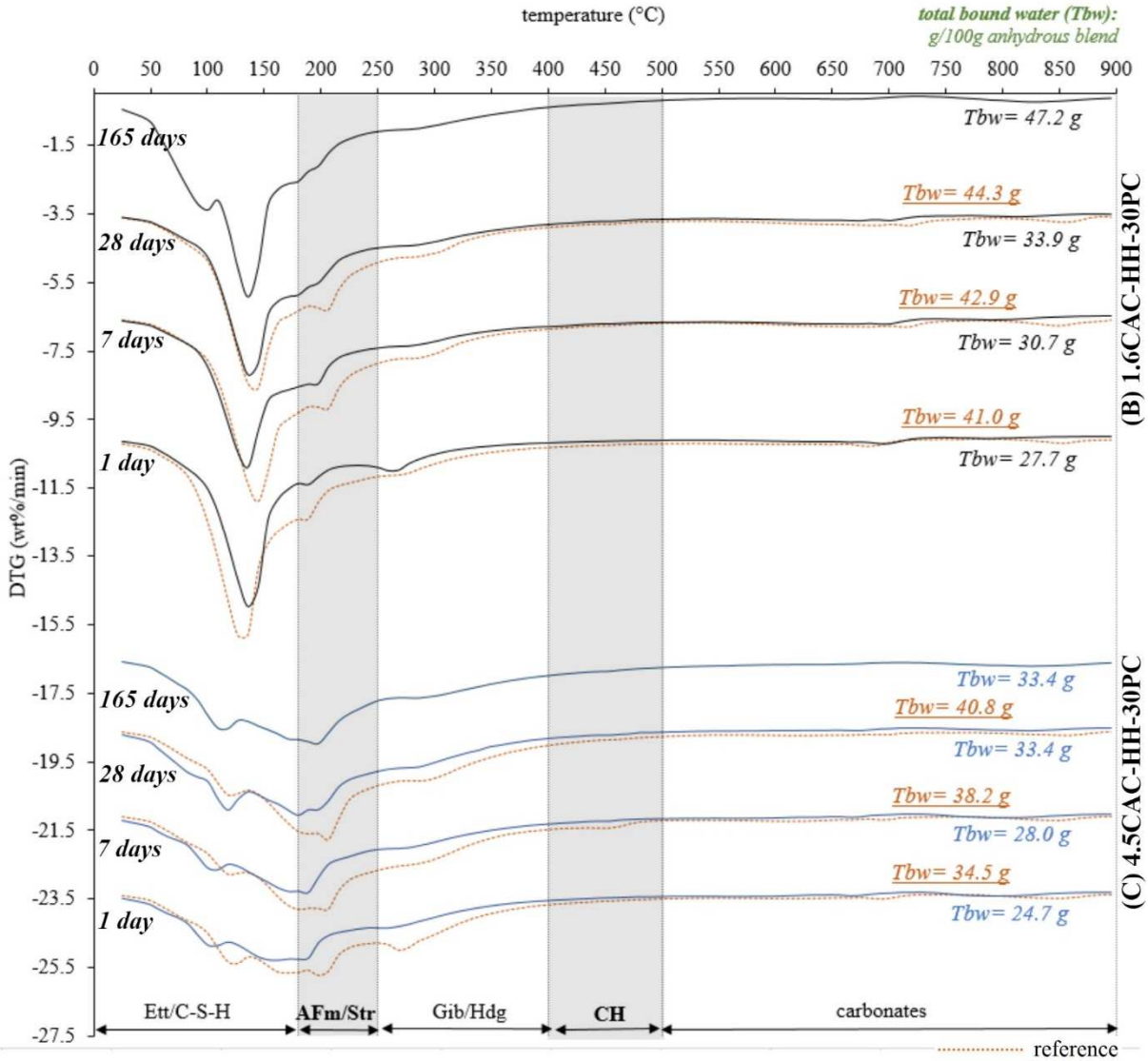

Figure 11 Evolution of the DTG curves of formulations (B)1.6CAC-HH-30PC, (C) 4.5CAC-HH-30PC and their corresponding cement references measured from paste samples after stopping the hydration at 1, 7, 28 and 165 days of curing. The different phases are abbreviated as follows: (Ett) ettringite, (CSH) C-S-H, (AFm) AFm, (Str) strätlingite, (Gib) gibbsite, (Hdg) hydrogarnet, and (CH) portlandite.

While the notable changes in the XRD and DTG patterns occur between 1 to 7 days for the formulation B, the variations in formulation C are more evident between 7 and 28 days of curing. Despite having a different hydrate phase assemblage as opposed to the C-S-H- dominated formulation B, the strätlingite-dominated formulation C similarly exhibits evolution chiefly in the range of $2\theta = 29°\text{-}30°$ (**Figure 10**). An increase in the amount of C-S-H is manifested by the peak shift from 101°C (ettringite) to 118°C

(C-S-H) in the DTG curves from 7 to 28 days of curing. Clear variations in the AFm-strätlingite region (**Figure 11**) are observed for both formulations B and C from 1 to 7 days and from 7 to 28 days of curing, respectively. The peaks in this region continue to change significantly for formulation C after 165 days of hydration. Assuming that these reactions are mainly influenced by the slag hydration, these findings could suggest that the CAC/HH ratio has an influence not only in the extent (as seen in XCT) but also in the kinetics of the slag reaction, such that the slag reacts faster in the PC-containing system with more HH content. Nevertheless, further evidence of the slag reaction complementary to the XCT results is warranted not only to affirm the slag reactivity but also to understand the mechanism of the slag hydration. It is also important to note that discerning the evolution of the AFm phases was not straightforward due to: (1) the poorly-ordered structure of some of the AFm phases (i.e. monosulfoaluminate [34]); (2) their variable structure; and (3) their reported sensitivity to desiccation during sample preparation which could lead to shifts at the diffraction peak patterns [35].

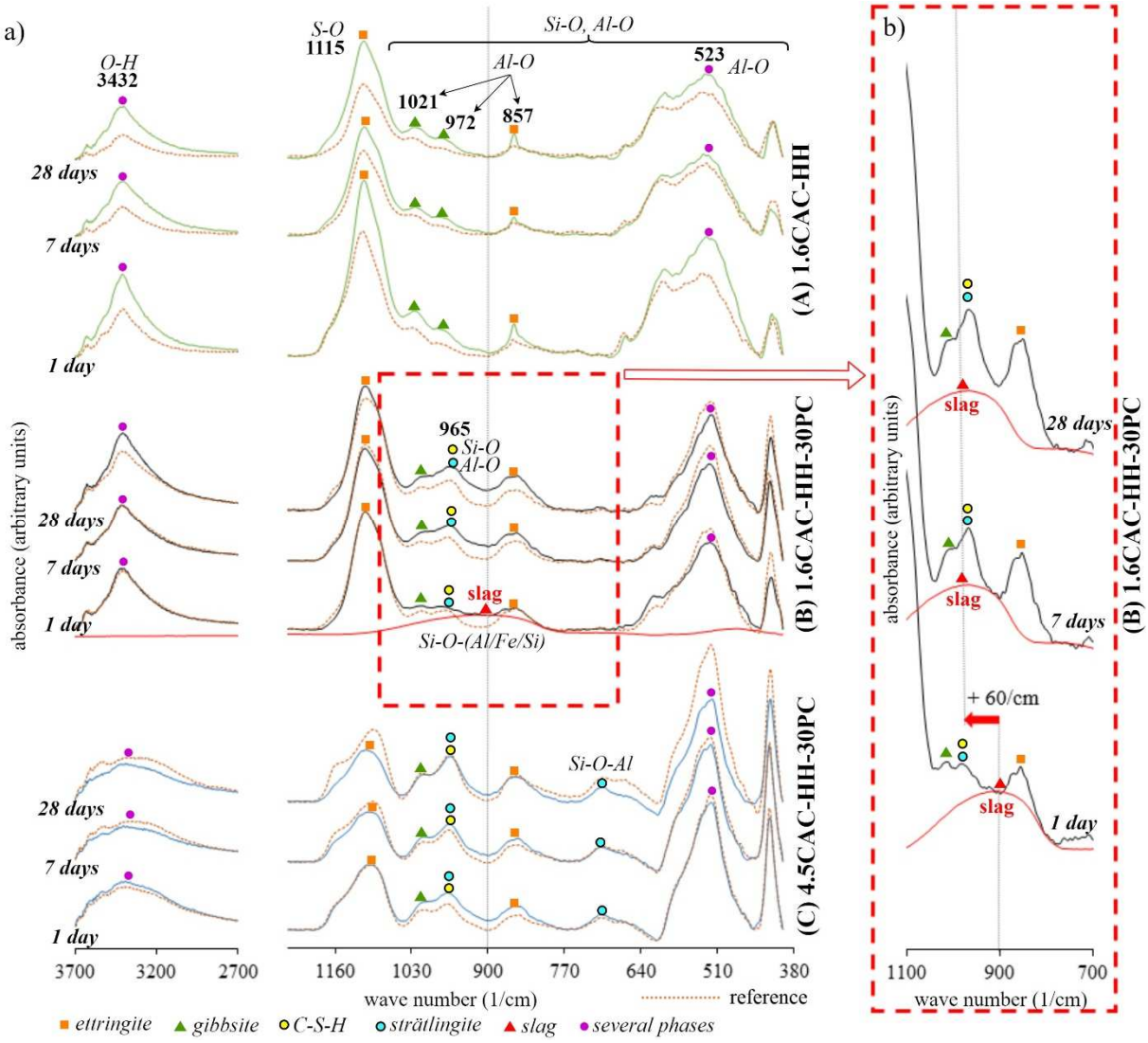

433

434 **Figure 12** ATR-FTIR spectra of the three formulations with their respective cement references
435 measured from paste samples after stopping the hydration at 1, 7 and 28 days of curing (a). The
436 previously presented ATR-FTIR spectra (in solid red line) of the raw slag used is superimposed with
437 intensity adjustment to the spectrum of (B) 1.6CAC-HH-30PC in an attempt to illustrate a possible
438 scenario of peak shift due to slag hydration (b)

439 **Table 4** presents the ATR-FTIR band assignments based on the distinct spectral peaks in **Figure 12**
440 observed from the hydrated paste samples. As previously mentioned, these results support the phase
441 assemblage of the three formulations proposed based on XRD and TGA analyses. The spectra for
442 formulation A are chiefly dominated by the asymmetric stretching band of S-O at 1115 cm^{-1} and the Al-
443 O vibration band at 523 cm^{-1} assigned to ettringite and gibbsite, respectively. Similar to the previous

techniques, no significant change in the spectrum over time was observed. For formulation B, the asymmetric stretching band of S-O for ettringite and C-S-H coincides at 1115 cm^{-1}. The additional peak marked at 965 cm^{-1} observed in formulation B is mainly attributed to the asymmetric Si-O-Si and O-Si-O stretching vibration bands of C-S-H not present in formulation A. On the other hand, formulation C is characterized by the Al-O vibration band at 965 cm^{-1}, Si-O-Al vibration band at 710 cm^{-1} and Al-O vibration band at 530 cm^{-1} all chiefly attributed to one of the dominant hydrate phases in this formulation: strätlingite. In addition to these bands, the Si-O-Al asymmetric stretching band at 1150 cm^{-1} assigned to strätlingite can be observed to cause the broadening of the peak centered at 1115 cm^{-1} particularly towards the higher wave number axis.

Table 4 FTIR band assignments based on the distinct spectral peaks observed from the hydrated paste samples. Due to the overlapping peaks in the complex phase assemblage, only the strong (s) intensity bands are designated to the different relevant phases. The data presented is compiled from several references [7,24,36–39] individually specified and compared to the spectra obtained in this study. The different phases are abbreviated as follows: (Ms) monosulfoaluminate, (Ett) ettringite, (Str) strätlingite, (CSH) C-S-H, (Gib) gibbsite, and (Hdg) hydrogarnet.

Bond	Primary contributor	Wave number (cm^{-1})	Reference
O-H	Ms/Ett/Str	3432	Horgnies et al., 2013 [24]
		1660	Horgnies et al., 2013 [24]
S-O	Ett/Ms	1115	Horgnies et al., 2013 [24]
Si-O-Al	Str	1150	Okoronkwo, Glasser 2016 [36]
		710	Zapanta et al., 2020 [39]
Si-O	CSH	965	Guan et al., 2013 [37]
	anhydrous silicates	521	Torréns-Martin et al., 2013 [7]
Al-O	Gib	1021	Schroeder 2002 [38]
		972	Schroeder 2002 [38]
		751	Schroeder 2002 [38]
	Str	965	Okoronkwo, Glasser 2016 [36]
	Hdg	810	Horgnies et al., 2013 [24]
	Ett	857	Horgnies et al., 2013 [24]
	Gib/Ms/Str/Hdg	523-537	Horgnies et al., 2013 [24]
	Hdg	521	Torréns-Martin et al., 2013 [7]

Throughout the 28 days curing period, the only discernible change in the spectra in function of time among the three formulations is observed for formulation B in the proximity of the Si-O asymmetric stretching band at 965 cm^{-1} assigned primarily to C-S-H. This same region coincides with the Si-O-T

463 (where T could be Al, Fe or Si) asymmetric stretching vibration band of the raw slag previously
464 presented in **Figure 2** and further illustrated in **Figure 12**a by superimposing the spectrum of the raw
465 slag in the 1-day-spectrum of formulation B. It is proposed that a peak displacement demonstrated in
466 **Figure 12**b could have occurred more evidently between 1 and 7 days in formulation B where the slag
467 hydration degree is the highest according to XCT estimation (**Figure 6**). The disappearance of the gaps
468 (red double arrows) in the superimposed spectra in **Figure 13** could be interpreted as a possible
469 consequence of peak displacement towards the higher wave number, causing the unreacted slag peaks
470 to be concealed in the adjacent areas. This suggested peak shift is postulated to be related to the
471 mechanism reported in Siakati et al., 2020 [22] indicating the reactivity of Fe silicate slags as precursors
472 to inorganic polymers. It was explained that this peak shift could be related to the partial oxidation of
473 the Fe^{2+} in the slag to Fe^{3+} incorporated in the silicate networks and similarly to the incorporation of Fe
474 in trioctahedral layers of the binder [22]. This has also been noted to be accompanied by a slight shift of
475 the Al-O peak to a lower wave number as the Fe atoms partially replace Al thereby distorting the lattice.
476 The higher atomic mass of Fe (55.8 amu) versus Al (27 amu) and the changes in the number of non-
477 bridging oxygen (NBO) are described as the principal factors making the vibrational frequency (or the
478 wave number in FTIR) lower [40,41]. While this peak shift is easily distinguishable in inorganic
479 polymers, the complexity of the spectra of the cement components (CAC and PC) and their hydrate
480 products makes the analysis more intricate for the systems investigated in this study. It is possible that
481 the observed changes in the spectra originate from other hydration reactions occurring simultaneously.
482 This limitation calls for the need to identify and characterize the actual hydrate phase incorporating Fe,
483 the main and distinct component of the slag, using TEM presented in the following section.
484

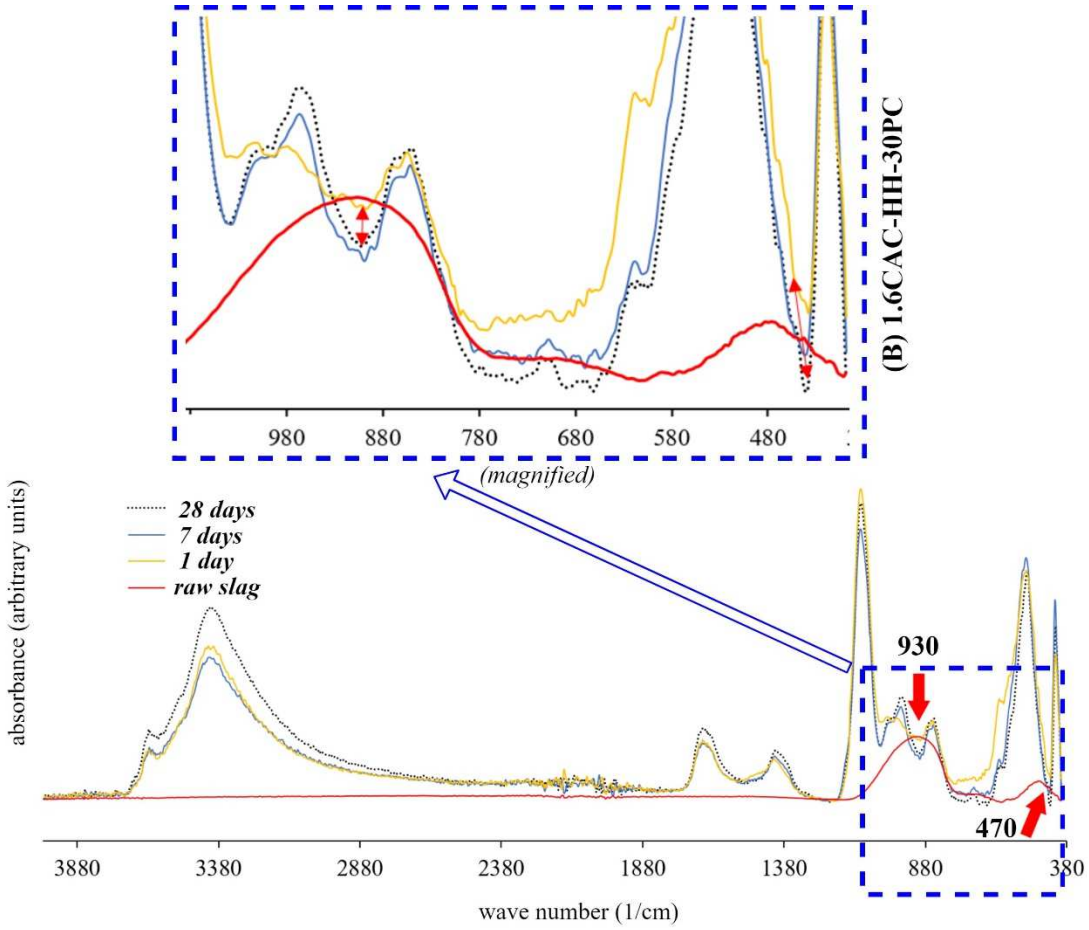

485

486 **Figure 13** Superimposed ATR-FTIR spectra of formulation (B) 1.6CAC-HH-30PC and the raw slag;
487 with an insert graph focusing on the region where the peaks of the unreacted slag are expected. It aims
488 to highlight how the gaps (red double arrows) formed over time could be an evidence of the proposed
489 peak-displacement scenario signifying slag hydration.

490 **3.4 The fate of Fe in the hydration**

491 Several TEM images of the slag-containing paste formulations at different curing ages are presented in
492 this section. The percentages indicated pertain to the elemental atomic composition estimated from EDS
493 analysis, unless otherwise specified. Most of the selected images show phases where Fe is detected in
494 the hydrated samples. For all 3 formulations, there was no evidence of Fe incorporated in ettringite,
495 strätlingite, nor in AFm crystalline phases contrary to the stable Fe-bearing hydrates suggested in
496 previous studies [42,43]. Instead, Fe was detected in intermixed hydrate gels with distinct compositions
497 mainly associated with Ca, Al and Si. In the following analysis, the term "gel" is used to describe the
498 Fe-containing intermixed phase considering its morphology and poor crystallinity. Although the gel is

clearly a part of the solid binder, the use of this term is adapted from Cuesta et al., (2017) [44] and related literature [45,46] where amorphous aluminum hydroxide gels are characterized in calcium sulfoaluminate cement systems.

The atomic composition of the marked areas in the TEM images estimated with the EDS analysis can be referred to in **Table A.1 (Appendix)**. Only the atomic percentage of Fe is indicated in the images to avoid interpretations implying direct quantitative correlation of the estimated values to the absolute composition of the phases. Aside from the technique's inability to detect or accurately quantify elements with low atomic mass number [47], it is critical to highlight the sensitivity of the hydrates in contact with the electron beams demonstrated in **Figure A.1 (Appendix)**.

In the TEM images of formulation A (**Figure 14**), the general phase assemblage viewed on the micro scale revealed needles of different sizes appearing to dominate the system. This needle-like morphology was also detected in the other formulations with atomic ratios confirmed through EDS (i.e. B9, C6, C7) typically corresponding to that of ettringite. However, no significant signals of Fe were detected in these needles. On the other hand, only <1% of Fe was estimated at 28 days in the Al-rich (**Figure 19**) gels in formulation A. After 180 days, the average Fe detected increased to about 3-4% while generally maintaining the ratio between the other elements.

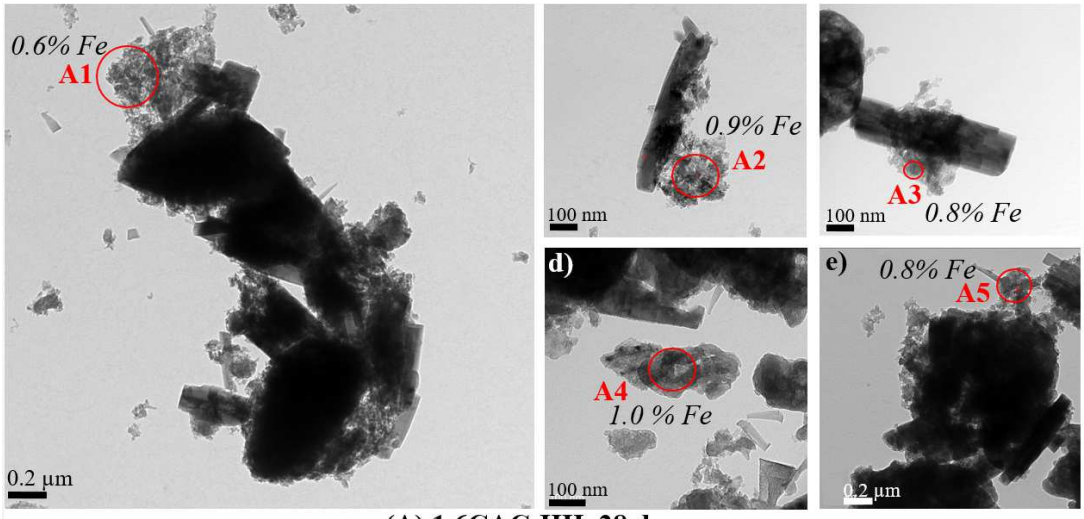

Figure 14 Selected TEM images focused on hydrate gels from the (A) 1.6CAC-HH paste sample after 28 days of hydration

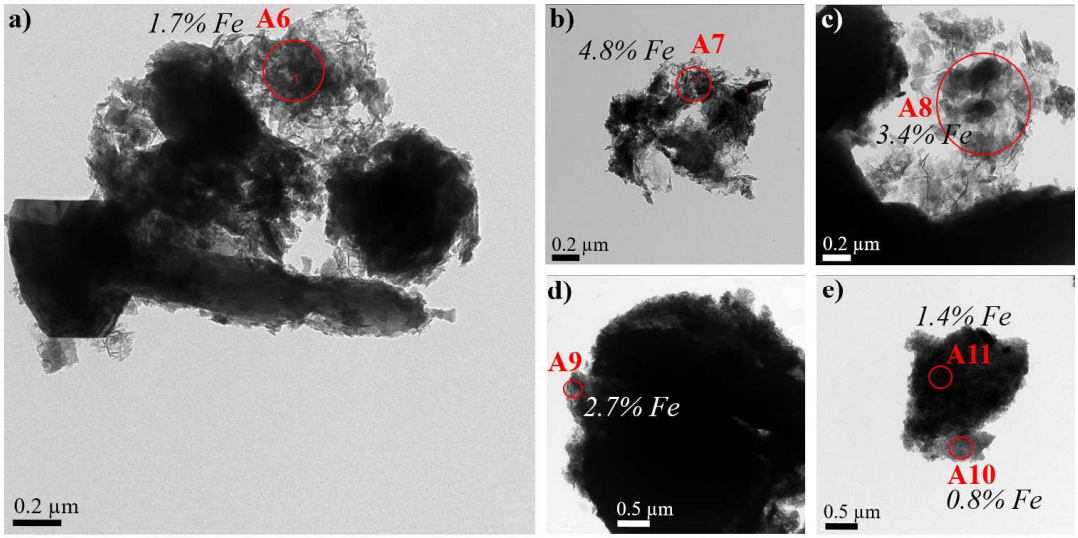

Figure 15 Selected TEM images focused on hydrate gels from the (A) 1.6CAC-HH paste sample after 180 days of hydration

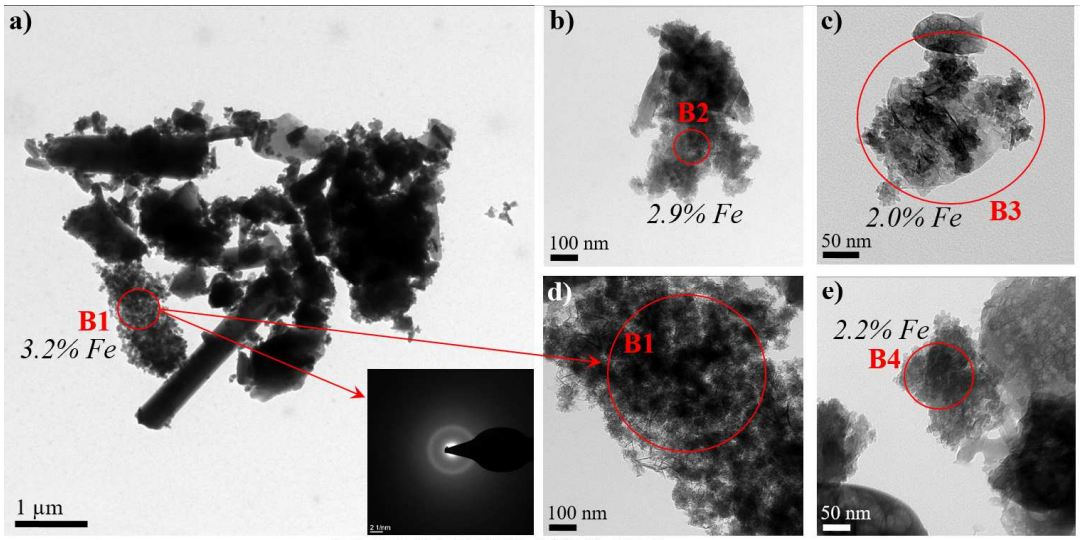

(B) 1.6CAC-HH-30PC_28 days

Figure 16 Selected TEM images focused on hydrate gels from the (B) 1.6CAC-HH-30PC paste sample after 28 days of hydration. The area diffraction pattern of the gel B1 is also presented in the lower right corner of (a)

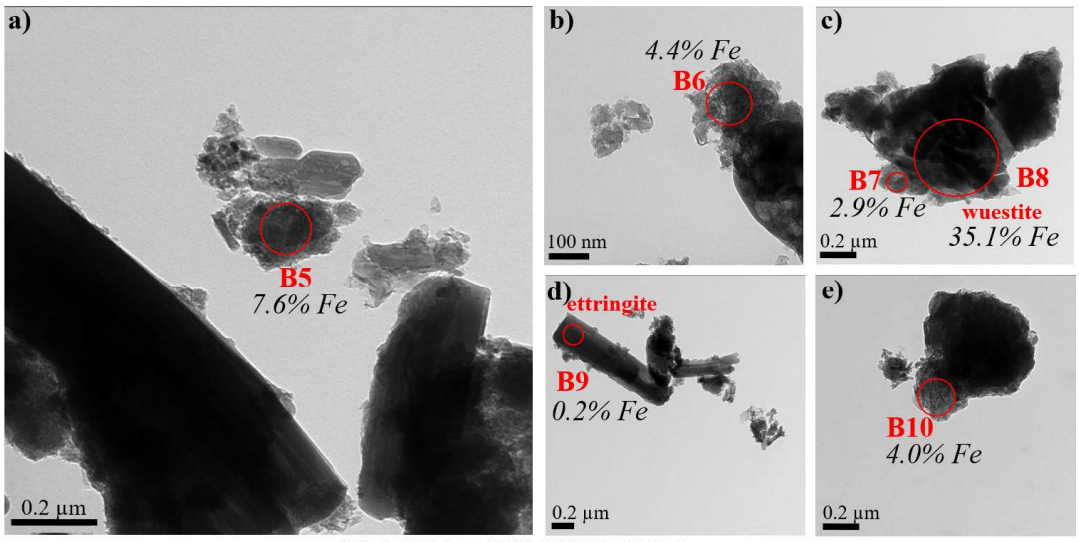

(B) 1.6CAC-HH-30PC_150 days

Figure 17 Selected TEM images from the (B) 1.6CAC-HH-30PC paste sample after 150 days of hydration

In the PC-containing blends, B and C, the gels where Fe was detected exhibited granular (i.e. B4, B6) and foil-like or fibrous (i.e. C1, C3) morphologies similar to those previously reported for C-S-H [48]. Having detected Ca, Al, and Si (see Appendix) in these hydrate gels, it is convenient to associate them to C-S-H at first glance. The selected electron diffraction pattern for B1 (**Figure 16**) also confirmed the poorly-crystalline to amorphous nature of this phase with the absence of clear diffraction spots.

However, compared to C-S-H, the Al estimated was significantly higher depicted in the ternary diagram in **Figure 19**. In the first 28 days of hydration, slightly higher signals for Fe (≈ 2-4%) were detected during the EDS analysis for the gels in formulation B compared to those in formulations A (< 1%) and C (1-2%). While this could be supported by the higher slag hydration degree in formulation B estimated through XCT (**Figure 6**), the differences in these values from the EDS analysis might be too small to draw accurate conclusions. Towards 150 days of curing (**Figure 17**), a more significant increase in Fe signal (3-8%) was observed in the gels. This could be a better, though indirect, indication of higher slag hydration at longer curing time parallel to those proposed from the previous techniques in this study.

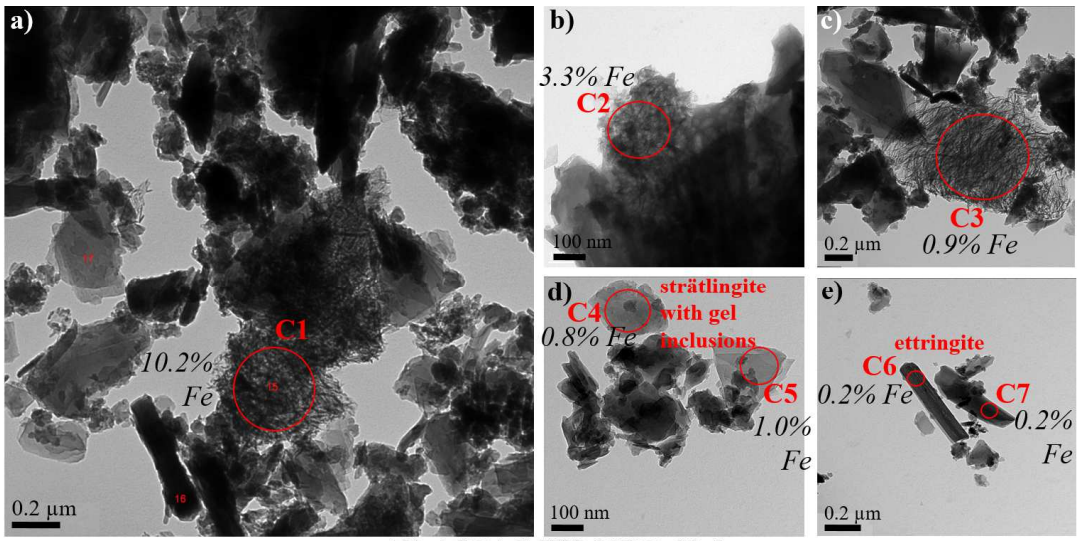

(C) 4.5CAC-HH-30PC_28 days

Figure 18 Selected TEM images from the (C) 4.5CAC-HH-30PC paste sample after 28 days of hydration

Furthermore, characteristic plate-like morphology corresponding to strätlingite was abundantly detected in formulation C, supporting the general phase assemblage proposed using the earlier techniques. Although monosulfoaluminate can also exhibit a similar plate-like morphology, it was verified through EDS analysis that those abundantly observed in the samples and marked in the images were strätlingite. **Figure 18** d shows plates of strätlingite (C4 and C5) with very low signals of Fe likely coming from the small inclusions of the hydrate gels in the same analytical volume. Unreacted wüstite from the raw slag in its distinct dendritic structure was also observed (**Figure 17** B8) intermixed with other phases. The presence of wüstite highlights the earlier remarks that only the (92 wt%) amorphous fraction of the slag is dissolving during the hydration [18]. EDS analysis on a region of Fe-containing hydrate gel (**Figure**

553 **17** B7) in close proximity with the wüstite demonstrates the highly contrasting Fe signals detected
554 between the crystalline fraction of the unreacted slag (wüstite) and the hydrate gel. This demonstrates
555 the precision of the EDS in analyzing different phases on a nano scale. While the intermixing of phases
556 due to the complex nature of the samples could not be completely eliminated, TEM still yields more
557 precise analysis compared to the SEM used in the previous study [18]. In order to further increase this
558 precision, the future work of the authors will be focused on characterizing these gels by creating nano
559 scale elemental maps using a scanning transmission electron microscopy (STEM). This is also expected
560 to detect any inhomogeneity in the distribution of the Fe within the gels considering that in some of
561 these phases, thicker regions only several nanometers in size (i.e. A8 in **Figure 15**) could be seen
562 enfolded within the matrix.
563 Finally, the atomic compositions of the hydrate gels (with 1-12% Fe) from the three formulations are
564 plotted in a ternary diagram of Ca-Si-Al in **Figure 19**. It can be seen that the gels from the PC-containing
565 formulations (B and C) could be grouped in a separate cluster from those of formulation A without PC.
566 The former appears to incorporate Fe in Ca-Al-Si rich hydrate gels while the latter in Al-rich gels. As
567 the hydration progress from 28 days to 150/180 days, the gels display a general tendency to move
568 towards region of lower Ca content. A similar trend on decreasing Ca/Si ratio in C-S-H has been
569 previously observed with the addition of siliceous SCM [49–51]. This trend could be linked to a similar
570 mechanism as in the Fe uptake in the interlayer of C-A-S-H gels in octahedral coordination,
571 demonstrated in Mancini et al., 2020 using ^{29}Si NMR and XAS spectroscopy [52]. However, the Al
572 content found in these gels was excessively elevated compared to those previously reported [53,54] to
573 be thermodynamically stable for C-A-S-H gels shown in **Figure 19**. This once again challenges the
574 homogeneity of the Fe-containing gels, implying that there might still be intermixing on the nano scale
575 and that other Fe-incorporating hydrate phases might remain unidentified within the gel matrix. Apart
576 from the aforementioned limitations of the TEM, the number of data points in the ternary diagram is
577 also most likely insufficient to reveal the identity of this phase. Nonetheless, the results of the
578 investigation draws the focus on the hydrate gels rather than on the reported [42,43] Fe-containing
579 crystalline phases (i.e. ettringite, AFm, hydrogarnet). No evidence of Fe incorporation in the later phases
580 was encountered using TEM in the cement systems studied. It is possible that other factors, such as the

presence of minor impurities and the kinetics of hydration, could have an impact to the hydration mechanism of the slag causing the difference in the fate of Fe from the aforementioned reports based on synthetic and modelled systems, versus that in the blends presented in this study.

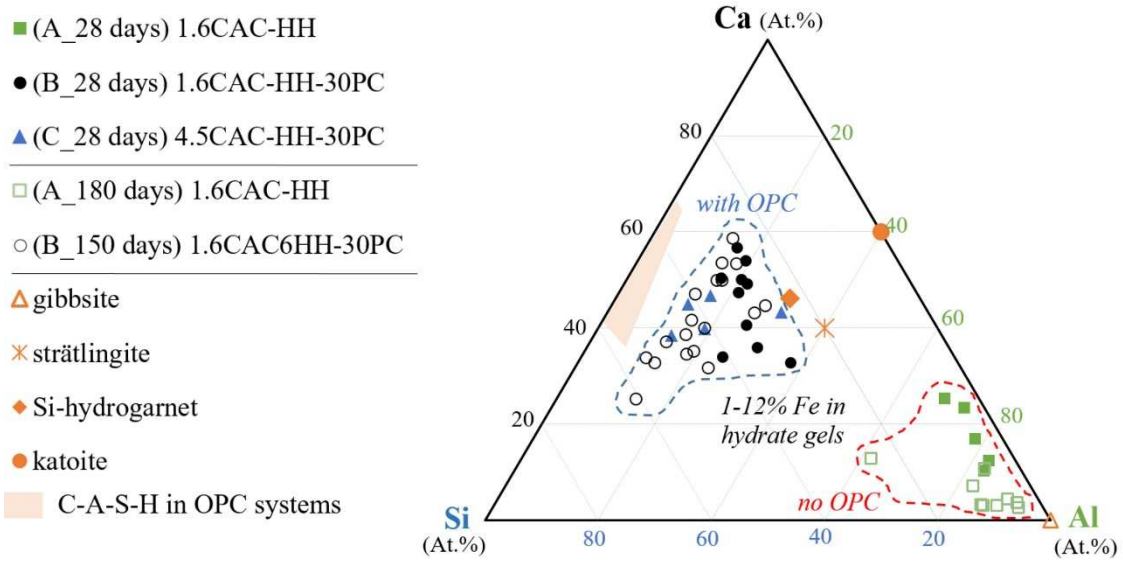

Figure 19 Ternary diagram of Fe-containing hydrate gels with 1-12% Fe observed using TEM. The values are calculated from the Ca, Si and Al atomic composition from TEM-EDS normalized to 100%. Reference points for gibbsite, strätlingite, katoite and Si-hydrogarnet are added in the diagram based on their empirical formula while the C-A-S-H region is estimated based on the reported stable composition in Portland cement system [54].

4 Conclusions

This study provided abundant information on the properties of CAC-based ternary binders incorporating Fe-rich NFM slag. It demonstrated the influence of PC addition to the slag hydration; highlighted the effect of slag addition to the dimensional stability of mortars; and finally provided insights in the fate Fe during hydration.

The evolution of the mechanical strength was consistent with the estimated degree of slag hydration from XCT. The slag-containing formulation B, with 30 wt% PC and a lower CAC/HH ratio at 1.6, exhibited the highest strength development trend relative to its reference formulation over 180 days of curing. For the same formulation, the highest degree of slag hydration after 28 days at 33 % has also been estimated using XCT. The addition of PC in two of the formulations in this study resulted in higher estimated slag hydration degree and an overall increase in the mechanical strength relative to their

reference formulations in the first 28 days. However, the PC addition did not seem to alter the overall hydration degree and mechanical performance at longer curing ages (≈ 6 months).

Furthermore, the slag addition contributed to the dimensional stability of the mortars particularly in the formulations where over-expansion was observed. While this improved stability was mostly due to the dilution of the more reactive components (CAC, PC and HH) in the dry mix, this positive contribution of the slag addition proved to be critical for the physical property of the binders.

On the other hand, the chemical contribution of the slag hydration was investigated by following the phase assemblage evolution of paste samples over time. Results from several characterization techniques indicated that the three formulations studied were governed by distinct hydrate systems, namely:

- **(A) 1.6CAC-HH** – dominated by ettringite and gibbsite throughout the curing period
- **(B) 1.6CAC-HH-30PC** – dominated by ettringite and gibbsite; strätlingite is increasing over time; possibly with C-S-H
- **(C) 4.5CAC-HH-30PC**– dominated by strätlingite and monosulfoaluminate; possibly with C-S-H

Despite the abundance of information from XCT, TGA and ATR-FTIR, it was not possible to clearly define the impact of these different hydrate systems; nor to identify the fate of Fe from the slag during hydration only based on these techniques. For this reason, TEM-EDS analysis was employed to identify and characterize the hydrate phase/s incorporating Fe. For all the 3 formulations, there was no evidence of Fe uptake in ettringite, strätlingite, nor in other AFm phases contrary to those reported in previous studies on synthetic and modelled systems. Instead, Fe was detected in hydrated gels grouped into two clusters: Al-rich gels in formulation A (no PC addition); and intermixed hydrate gels associated with Ca, Al and Si in formulations B and C (with 30 wt% PC). Further complementary analyses remain crucial in describing the structure of these gels particularly the role of Fe in the network, which will be the focus of an upcoming study.

5 Acknowledgements

J. Astoveza is grateful for receiving funding as an early-stage researcher of the SOCRATES Project under the European Union Framework Program for Research and Innovation Horizon 2020 Grant

Agreement No.721385 (EU MSCA-ETN SOCRATES; project website: http://etn-socrates.eu). The authors would also like to acknowledge Tobias Hertel and Jeroen Soete of KU Leuven for their valuable assistance in performing the ATR-FTIR and XCT, respectively; and Vincent Hallet of KU Leuven for his review of the paper.

6 References

[1] K.L. Scrivener, J.-L. Cabiron, R. Letourneux, High-performance concretes from calcium aluminate cements, Cement and Concrete Research 29 (1999) 1215–1223.

[2] W. Sand, T. Dumas, S. Marcdargent, Accelerated Biogenic Sulfuric-Acid Corrosion Test for Evaluating the Performance of Calcium-Aluminate Based Concrete in Sewage Applications, in: J.R. Kearns, B.J. Little (Eds.), Microbiologically Influenced Corrosion Testing, ASTM International, 100 Barr Harbor Drive, PO Box C700, West Conshohocken, PA 19428-2959, 1994, 234-234-16.

[3] H. Justness, Rapid repair of airfield runway in cold weather using CAC mortar, in: Calcium Aluminate Cements: Proceedings of the centenary conference, 365–372 IHS BRE Press, 2008.

[4] E.G. Moffatt, M.D.A. Thomas, Durability of Rapid-Strength Concrete Produced with Ettringite-Based Binders, ACI Materials Journal 115 (2018).

[5] L. Xu, P. Wang, G. de Schutter, G. Wu, Effect of calcium aluminate cement variety on the hydration of portland cement in blended system, J. Wuhan Univ. Technol.-Mat. Sci. Edit. (Journal of Wuhan University of Technology-Materials Science Ed.) 29 (2014) 751–756.

[6] J. Bizzozero, K. Scrivener, Hydration and microstructure of rapid-strength binders based on OPC accelerated by early ettringite formation, in: International Conference on Calcium Aluminates, Avignon, France, May 2014.

[7] D. Torréns-Martín, L. Fernández-Carrasco, M.T. Blanco-Varela, Conduction calorimetric studies of ternary binders based on Portland cement, calcium aluminate cement and calcium sulphate, Journal of Thermal Analysis and Calorimetry 114 (2013) 799–807.

[8] J. Nehring, J. Neubauer, S. Berger, F. Goetz-Neunhoeffer, Acceleration of OPC by CAC in binary and ternary systems: The role of pore solution chemistry, Cement and Concrete Research 107 (2018) 264–274.

[9] A.C.A. Rego, F.A. Cardoso, R.G. Pileggi, Ternary system Portland cement-calcium aluminate cement-calcium sulfate applied to self-leveling mortar: a literature review, Cerâmica 67 (2021) 65–82.

[10] E. Henry-Lanier, B. Espinosa, C. Eychenne-Baron, Environmental footprint of calcium aluminate cements (CAC), in: C.H. Fentiman, R. Mangabhai, K. Scrivener (Eds.), Internation Conference on Calcium Aluminate Cements Avignon, 2014.

[11] M. Burteaux, "Laitiers de haut fourneau," Techniques de l'Ingénieur. no. M 7 425 (1995).

[12] E. Qoku, Characterization and quantification of crystalline and amorphous phase assemblage in ternary binders during hydration: PhD Dissertation, TU Bergakademie Freiberg, 2019.

[13] Y. Abzaev, A. Gnyrya, S. Korobkov, K. Gauss, A. Boyarintsev, S. Tomrachev, Thermodynamic modeling of Portland cement without mineral additives, J. Phys.: Conf. Ser. 1145 (2019) 12016.

[14] J. Bizzozero, Hydration and dimensional stability of calcium aluminate cement based systems. PhD Dissertation, Laboratoire Des Matériaux de Construction, École Polythechnique Fédérale de Laussane, Lausanne, Switzerland, 2014.

[15] G. Van-Rompaey, Etude de la réactivité des ciments riches en laitier, à basse température et à temps court, sans ajout chloruré (PhD thesis): Université Libre de Bruxelles (2006).

[16] J. Astoveza, A. Abadias, R. Soth, R. Trauchessec, M. Reuter, Y. Pontikes, Industrial by-products as non-conventional supplementary cementitious material: YRSB19 - iiSBE Forum of Young Researchers in Sustainable Building, (2019).

[17] P.T. Jones, D. Geysen, Y. Tielemans, S. van Passel, Y. Pontikes, B. Blanpain, M. Quaghebeur, N. Hoekstra, Enhanced Landfill Mining in view of multiple resource recovery: A critical review, Journal of Cleaner Production 55 (2013) 45–55.

[18] J. Astoveza, R. Trauchessec, R. Soth, Y. Pontikes, Properties of calcium aluminate blended cement incorporating iron-rich slag: Evolution over a curing period of 1 year, Construction and Building Materials 282 (2021) 122569.

[19] J. Astoveza, R. Trauchessec, R. Soth, J. Salminen, Y. Pontikes, Assessing the reactivity of industrial by-products in calcium aluminate cement-based formulations, in: A. Malfliet, A. Peys, A. Di Maria (Eds.), Proceedings of the 6th International Slag Valorisation Symposium, 1-5 April 2019, Mechelen, Belgium: Science, innovation & entrepreneurship in pursuit of a sustainable world, KU Leuven, Materials Engineering, Leuven, 2019.

[20] J. Srodon, V.A. Drits, D.K. McCarty, J.C.C. Hsieh, D.D. Eberl, Quantitative X-ray diffraction analysis of clay bearing rocks from random preparations. Clays and Clay Minerals Vol 49, No 6 (2001) 514–528.

[21] I. Garcia-Lodeiro, K. Irisawa, F. Jin, Y. Meguro, H. Kinoshita, Reduction of water content in calcium aluminate cement with/out phosphate modification for alternative cementation technique, Cement and Concrete Research 109 (2018) 243–253.

693 [22] C. Siakati, A.P. Douvalis, P. Ziogas, A. Peys, Y. Pontikes, Impact of the solidification path of
694 FeO x –SiO 2 slags on the resultant inorganic polymers, Journal of the American Ceramic
695 Society 103 (2020) 2173–2184.

696 [23] Y. Liu, A. Wang, J.J. Freeman, Raman, MIR, and NIR spectroscopic study of calcium sulfates:
697 gypsum, bassanite, and anhydrite: 40th Lunar and Planetary Science Conference (2009).

698 [24] M. Horgnies, J.J. Chen, C. Bouillon, Overview about the use of Fourier Transform Infrared
699 spectroscopy to study cementitious materials, in: C.A. Brebbia, A.A. Mammoli, A. Klemm
700 (Eds.), Materials Characterisation VI, WIT PressSouthampton, UK, 2013, pp. 251–262.

701 [25] H. Nguyen, P. Kinnunen, K. Gijbels, V. Carvelli, H. Sreenivasan, A.M. Kantola, V.-V. Telkki,
702 W. Schroeyers, M. Illikainen, Ettringite-based binder from ladle slag and gypsum – The effect of
703 citric acid on fresh and hardened state properties, Cement and Concrete Research 123 (2019)
704 105800.

705 [26] J. Astoveza, R. Trauchessec, R. Soth, Quantifying the Degree of Fe-rich Slag Hydration in
706 Calcium Aluminate Blended Cement by Image Analysis of SEM-BSE and XCT (oral
707 presentation), Espoo, Finland, 2019.

708 [27] E. Berodier, K. Scrivener, Understanding the Filler Effect on the Nucleation and Growth of C-S-
709 H, Journal of the American Ceramic Society 97 (2014) 3764–3773.

710 [28] Maier S., Ternary system: calcium aluminate cement – portland cement – gypsum, in: C.H.
711 Fentiman, R. Mangabhai, K. Scrivener (Eds.), Internation Conference on Calcium Aluminate
712 Cements Avignon, 2014, pp. 511–526.

713 [29] C. Li, J. Li, A. Telesca, D. Marchon, K. Xu, M. Marroccoli, Z. Jiang, P.J.M. Monteiro, Effect of
714 polycarboxylate ether on the expansion of ye'elimite hydration in the presence of anhydrite,
715 Cement and Concrete Research 140 (2021) 106321.

716 [30] C. Yu, W. Sun, K. Scrivener, Degradation mechanism of slag blended mortars immersed in
717 sodium sulfate solution, Cement and Concrete Research 72 (2015) 37–47.

718 [31] F. Song, Z. Yu, F. Yang, Y. Lu, Y. Liu, Microstructure of amorphous aluminum hydroxide in
719 belite-calcium sulfoaluminate cement, Cement and Concrete Research 71 (2015) 1–6.

720 [32] G.W. Scherer, Factors affecting crystallization pressure, in: International RILEM Workshop on
721 Internal Sulfate Attack and Delayed Ettringite Formation, RILEM Publications SARL,
722 04/09/2002 - 06/09/2002, pp. 139–154.

723 [33] G. Puerta-Falla, M. Balonis, G. Le Saout, N. Neithalath, G. Sant, The Influence of Metakaolin on
724 Limestone Reactivity in Cementitious Materials, in: K. Scrivener, A. Favier (Eds.), Calcined
725 Clays for Sustainable Concrete, Springer Netherlands, Dordrecht, 2015, pp. 11–19.

[34] P. Feng, C. Miao, J.W. Bullard, Factors influencing the stability of AFm and AFt in the Ca-Al-S-O-H system at 25 °C, Journal of the American Ceramic Society 99 (2016) 1031–1041.

[35] T. Matschei, B. Lothenbach, F.P. Glasser, The AFm phase in Portland cement, Cement and Concrete Research 37 (2007) 118–130.

[36] M.U. Okoronkwo, F.P. Glasser, Strätlingite: compatibility with sulfate and carbonate cement phases, Materials and Structures 49 (2016) 3569–3577.

[37] W. Guan, F. Ji, Q. Chen, P. Yan, L. Pei, Synthesis and Enhanced Phosphate Recovery Property of Porous Calcium Silicate Hydrate Using Polyethyleneglycol as Pore-Generation Agent, Materials (Basel, Switzerland) (2013) 2846–2861.

[38] P.A. Schroeder, Infrared Spectroscopy in Clay Science Schroeder, P.A. (2002) Infrared Spectroscopy in clay science: In CMS Workshop Lectures, Vol. 11, Teaching Clay Science, A. Rule and S. Guggenheim, eds., The Clay Mineral Society, Aurora, CO, 181-206, in: A.C. Rule, S. Guggenheim (Eds.), Teaching clay science, Clay Minerals Society, Aurora, CO, 2002, pp. 182–205.

[39] J.F. Zapata, H.A. Colorado, M.A. Gomez, Effect of high temperature and additions of silica on the microstructure and properties of calcium aluminate cement pastes, Journal of Sustainable Cement-Based Materials 9 (2020) 323–349.

[40] C. Adhikari, Seminar on IR Spectrocopy: Theory, 2016.

[41] A. Peys, C.E. White, H. Rahier, B. Blanpain, Y. Pontikes, Alkali-activation of CaO-FeOx-SiO2 slag: Formation mechanism from in-situ X-ray total scattering, Cement and Concrete Research 122 (2019) 179–188.

[42] B.Z. Dilnesa, E. Wieland, B. Lothenbach, R. Dähn, K.L. Scrivener, Fe-containing phases in hydrated cements, Cement and Concrete Research 58 (2014) 45–55.

[43] G. Möschner, B. Lothenbach, F. Winnefeld, A. Ulrich, R. Figi, R. Kretzschmar, Solid solution between Al-ettringite and Fe-ettringite (Ca6[Al1−xFex(OH)6]2(SO4)3•26H2O), Cement and Concrete Research 39 (2009) 482–489.

[44] A. Cuesta, A.G. de La Torre, I. Santacruz, P. Trtik, J.C. da Silva, A. Diaz, M. Holler, M.A.G. Aranda, Chemistry and Mass Density of Aluminum Hydroxide Gel in Eco-Cements by Ptychographic X-ray Computed Tomography, J. Phys. Chem. C 121 (2017) 3044–3054.

[45] Y. Zhang, J. Chang, Microstructural evolution of aluminum hydroxide gel during the hydration of calcium sulfoaluminate under different alkali concentrations, Construction and Building Materials 180 (2018) 655–664.

[46] M. Ben Haha, F. Winnefeld, A. Pisch, Advances in understanding ye'elimite-rich cements, Cement and Concrete Research 123 (2019) 105778.

[47] J.E. Rossen, K.L. Scrivener, Optimization of SEM-EDS to determine the C–A–S–H composition in matured cement paste samples, Materials Characterization 123 (2017) 294–306.

[48] I. Techer, D. Bartier, P. Boulvais, E. Tinseau, K. Suchorski, J. Cabrera, A. Dauzères, Tracing interactions between natural argillites and hyper-alkaline fluids from engineered cement paste and concrete: Chemical and isotopic monitoring of a 15-years old deep-disposal analogue, Applied Geochemistry 27 (2012) 1384–1402.

[49] J.E. Rossen, B. Lothenbach, K.L. Scrivener, Composition of C–S–H in pastes with increasing levels of silica fume addition, Cement and Concrete Research 75 (2015) 14–22.

[50] F. Avet, E. Boehm-Courjault, K. Scrivener, Investigation of C-A-S-H composition, morphology and density in Limestone Calcined Clay Cement (LC3), Cement and Concrete Research 115 (2019) 70–79.

[51] F. Deschner, F. Winnefeld, B. Lothenbach, S. Seufert, P. Schwesig, S. Dittrich, F. Goetz-Neunhoeffer, J. Neubauer, Hydration of Portland cement with high replacement by siliceous fly ash, Cement and Concrete Research 42 (2012) 1389–1400.

[52] A. Mancini, E. Wieland, G. Geng, R. Dähn, J. Skibsted, B. Wehrli, B. Lothenbach, Fe(III) uptake by calcium silicate hydrates, Applied Geochemistry 113 (2020) 104460.

[53] É.M. L'Hôpital, Aluminium and alkali uptake in calcium silicate hydrates (C-S-H), Lausanne, EPFL, 2014.

[54] I. Garcia-Lodeiro, A. Palomo, A. Fernández-Jiménez, D.E. Macphee, Compatibility studies between N-A-S-H and C-A-S-H gels. Study in the ternary diagram Na2O–CaO–Al2O3–SiO2–H2O, Cement and Concrete Research 41 (2011) 923–931.

Appendix

The table below lists the atomic compositions estimated from the EDS analysis of marked areas in the TEM images presented in **Figures 14-18**. The absence of measurement due to undiscernible peaks for some of the elements are indicated by "–".

Table A. 1 The atomic composition of the marked areas in the TEM images (Figures 14-18) estimated with the EDS analysis

At. %	Fe	Ca	Al	Si	S	Mg	K + Na	O	Sum
A1	0.6	5.1	34.2	2.0	1.3	1.3	0.1	55.4	100.0
A2	0.9	6.6	30.2	1.9	1.3	1.4	0.1	57.6	100.0
A3	0.8	3.6	28.9	2.3	1.0	1.1	0.2	62.1	100.0
A4	1.0	9.7	26.2	2.3	1.9	0.8	0.2	57.9	100.0
A5	0.8	13.8	43.0	2.1	5.4	1.0	0.4	33.6	100.0
A6	1.7	5.0	24.0	9.9	1.8	1.4	1.0	55.4	100.0
A7	4.8	2.9	33.6	4.1	0.5	2.9	2.2	49.0	100.0
A8	3.4	6.2	48.6	3.7	1.4	1.3	0.1	35.1	100.0
A9	2.7	1.3	37.2	4.5	0.2	2.7	1.8	49.6	100.0
A10	0.8	0.9	33.3	1.6	0.4	2.0	1.0	60.0	100.0
A11	1.4	1.3	34.7	1.5	0.4	2.0	1.5	57.0	100.0
B1	3.2	10.4	6.6	8.6	0.3	–	–	70.9	100.0
B2	2.9	11.0	9.2	10.4	0.2	–	–	66.2	100.0
B3	2.0	9.1	10.5	8.2	0.2	–	–	70.0	100.0
B4	2.2	9.8	4.4	6.6	0.2	–	–	76.8	100.0
B5	7.6	17.3	6.6	17.8	0.8	0.4	0.7	48.7	100.0
B6	4.4	16.6	8.8	22.6	1.1	0.1	1.3	45.2	100.0
B7	2.9	9.9	4.1	16.2	0.5	0.2	0.9	65.3	100.0
B8	35.1	3.7	3.4	3.2	0.1	1.2	0.4	53.0	100.0
B9	0.2	24.5	8.1	1.2	6.7	0.0	0.6	58.8	100.0
B10	4.0	11.3	4.1	15.0	0.3	1.9	1.1	62.4	100.0
C1	10.2	16.2	7.7	16.8	0.8	5.5	0.5	42.4	100.0
C2	3.3	17.1	12.2	10.3	3.6	9.6	0.6	43.3	100.0
C3	0.9	15.7	5.6	19.5	0.7	0.1	0.5	57.0	100.0
C4	0.8	18.2	16.7	8.8	0.6	0.3	0.6	54.1	100.0
C5	1.0	16.7	16.1	8.9	0.5	0.7	0.5	55.7	100.0
C6	0.2	30.5	10.7	1.0	7.3	0.1	0.6	49.7	100.0
C7	0.2	29.8	9.2	1.2	7.8	0.0	0.8	51.1	100.0

It is important to note that these values should not be taken as quantitative measures of the composition of the phases. Rather, they are indicators of the average proportions of the elements interacting with the electron beam. Elements, particularly hydrogen and carbon, which are critical components of several

phases in the cement systems are too light (low atomic mass number) to be detected in the EDS analysis. Oxygen, also a light element, is often erroneously estimated.

Another important consideration in interpreting the atomic composition is the sensitivity of the hydrated samples in contact with the electron beams. This is demonstrated in **Figure A. 1** where gels are shown to disintegrate right after the EDS analysis. While this facilitates differentiation of the (more sensitive) hydrates from the anhydrous phases in the blend, this could also greatly modify the estimated atomic percentages as some of the components could possibly disintegrate even during the scan. Nonetheless, expressing the values in terms of atomic percentage allows calculation of molar/atomic ratios of relatively heavier elements especially Ca, Si and Al as in the ternary diagram (**Figure 19**). When presented in ratios, they become more reliable references for phase identification. The atomic percentage of Fe indicated in the following figures should be taken as an indicator of the presence of Fe rather than an absolute composition.

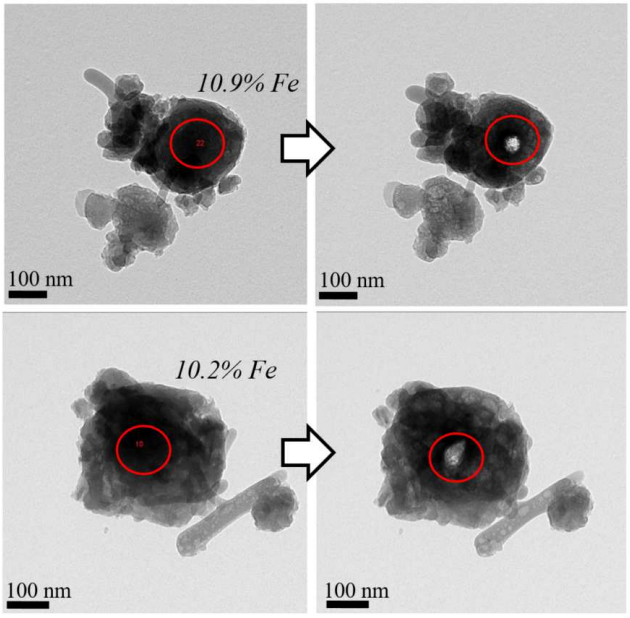

Figure A. 1 TEM images before and after EDS analysis of Fe-containing hydrate gels